Universiteit Gent

Faculteit Wetenschappen
Vakgroep Fysica en Sterrenkunde

Design of a glass resistive plate chamber for the upgrade of the Compact Muon Solenoid muon system

Author
Sander Vanheule

Promotor
Michael Tytgat

Supervisor
Alexis Fagot

15 June, 2013

Thesis submitted in partial fulfilment of the requirements for the degree of
Master of Science in Physics and Astronomy

Preface

During the past eight months, I have spent quite some time at the Institute of Nuclear Sciences (INW) working on my thesis, helping out with the construction of the RE/4/3 RPCs for CMS, and talking to the people — about physics and a multitude of other things — who have been my 'colleagues' during my final year as a physics student. I am greatly indebted to the faculty and its staff for the knowledge and experience I gathered during the five years of my enrolment as a student at Ghent University, and my parents for providing me with the opportunity of enjoying this education.

I have to thank everyone involved in the project. Although I risk forgetting some names, I would like to thank:

Alexis, who was often more of a co-worker than a supervisor throughout this project,
Michael, for directing us through the gRPC project and proofreading my thesis,
Nicolas, for helping out (with everything) when I was at CERN for the electronics measurement,
Simon, Patrick, Philippe, and Christophe for their advice and support on the more technical matters, and
Ken, for helping with the construction of the gRPC prototype.

Finally, a wholehearted "thank you" goes out to my RPC colleagues Alexis and Simon, my fellow master students Simon and Isabelle, and everyone else who made lunches, 4 o'clock breaks, and my time in general at the INW more enjoyable.

Contents

Introduction

During the 20^{th} century our understanding of subatomic physics has increased substantially. By the 1960s, experimentalist had already discovered an extensive list of particles. Until then, they had no comprehensive framework that described their observations, but several theories were maturing and being put together into what we now know as the Standard Model of particle physics. This allowed the high energy physics community to make predictions based on earlier observations. Up to this day, the Standard Model of particle physics is one of the theories that has been tested and confirmed to the highest precision. The Standard Model is not fully compatible with general relativity however, and badly understood observations such as dark matter hint that there should be 'new physics' still to be discovered.

The initial observations that led to the development of the Standard Model, the testing of its predictions afterwards, and looking for new physics, all require sources of energetic particles and the use of detectors. Early discoveries were made with cosmic rays, and these are still the only source for extremely energetic particles. Thanks to technical advances, we are now also able to construct machines that accelerate particles up to several TeV, allowing us to study rare events in more controlled environments. The Standard Model will be discussed in chapter 1, followed by a short introduction on detection principles of elementary particles.

At the Large Hadron Collider (LHC) in Geneva, protons are now accelerated up to 4 TeV, providing a centre-of-mass energy of 8 TeV. Starting from early 2013, the accelerator has been shut down to prepare the machine and its experiments to run at its design power of 14 TeV and luminosity of $10^{34}\,\text{cm}^{-2}\,\text{s}^{-1}$. The University of Ghent is part of the Compact Muon Solenoid (CMS) Collaboration running one of the detectors at LHC. We are providing a contribution to the analysis of the data on the topics of top quark physics and supersymmetry (SUSY). On the hardware side, we are contributing to the extension of the detector's muon system.

The contribution of Ghent to the hardware of CMS is in part focussed on resistive plate chambers (RPCs). These are thin gaseous detectors that will be explained in more detail in chapter 2. With the next scheduled update of LHC, the accelerator will see an increase in luminosity, but the current RPCs are not able to cope with the expected higher rates. Hence different groups are currently developing new types of detectors. RPCs are also used in the R&D program of the CALICE Collaboration, in which Ghent also takes part. CALICE aims to develop high granularity sampling calorimeters for use in future linear collider experiments. Chapter 1 will provide a short introduction on the CMS detector, and give some extra information on the goal of the CALICE Collaboration.

I have helped in the development of a prototype glass resistive plate chamber (gRPC), based on experiences of the Ghent group with the CMS and CALICE collaborations, covered in detail in chapter 5. Construction of this prototype is part of an effort to find suitable detectors that will be able to cope with the harsher environment at the LHC experiments, after its second upgrade around 2018. The gathered experience can then also be put to use in R&D for CALICE. This development has been performed in cooperation with A. Fagot, as part of his PhD thesis, and with K. Erpels, for his bachelor project.

Aside from the construction and characterisation of the gRPC prototype, my personal work has furthermore focussed on two aspects of its operation. First of all, I have worked on the resistive electrode coating discussed in chapter 3. I have looked at how the coating can be best applied, determined its desired properties, and characterised the final coatings used in our prototype. Secondly, I have done preliminary measurements at CERN with new, sensitive read-out electronics. Using more sensitive electronics provides an easy way of increasing the rate capabilities of a RPC, even without having to make significant changes to its design, thus contributing to our goal to develop a RPC for future use in CMS.

Chapter 1

Particle physics primer

Since the 1960s, the physics community has had a comprehensive theory that describes elementary particle physics: the Standard Model. Like any theory, the Standard Model has to be confirmed by experiment in order to be accepted as valid. Subatomic particles are however far too small to be observed directly by scientists. Therefore, it is important to know and understand how they interact with the matter of macroscopic systems. In this way, using our detector we are to be able to convert their presence into observable quantities, which allow us to characterise them.

1.1 The Standard Model

The Standard Model describes the dynamics of elementary particles. It is a mathematical formulation of the strong and the electroweak interactions, the latter breaking down into the better known electromagnetic and weak interactions. These interactions give rise to the forces that connect all known elementary particles. The electromagnetic interaction is the one we are most familiar with, since it lies at the basis a large part of the physics the influences our daily lives. The weak interaction mediates some forms of nuclear decays, while the rest of the nuclear realm is basically a result of the strong interaction.

The elementary particles described by the Standard Model can be divided into two groups: the bosons and the fermions. Matter is built up out of fermions, and interactions between these fermions happens by exchange of bosons. The fermions can be divided up into two groups: the leptons and quarks. The leptons are only affected by the electroweak interaction, while the quarks are also subjected to the strong interaction. A list of all the fermions is given in Table 1.1, along with their electrical charge, and a further subdivision into three generations. With the exception of the neutrinos, for each new generation, the mass of these particles increases substantially. Neutrinos are so light however, that until now we have only been able to put upper limits on their masses. For every particle in Table 1.1, an antiparticle exists with the exact same mass, but opposite charge, usually denoted with a bar, e.g. $\bar{\mathrm{u}}$. The bosons are listed in Table 1.2, along with their electric charge, and the interaction they mediate.

The quarks and charged leptons of the second and third generation, as well as the heavy bosons of the weak interaction, are more massive than some of the particles they can interact with. As a result, they will spontaneously decay into these lighter particles. The mass difference between the initial state — the heavy particle, and the final state — the collection of lighter particles, is then converted into kinetic energy

Table 1.1: List of elementary fermions. The charges are denoted in units of the elementary charge.

Type	Generation I	Generation II	Generation III	Charge
Charged leptons	e^-	μ^-	τ^-	-1
Neutrinos	ν_e	ν_μ	ν_τ	0
Up-type quarks	u	c	t	$\frac{2}{3}$
Down-type quarks	d	s	b	$-\frac{1}{3}$

Table 1.2: List of elementary bosons. The charges are denoted in units of the elementary charge.

Boson	Force	Interacting fermions	Charge
$W^{\pm}$	Weak	Quarks, leptons	± 1
Z	Weak	Quarks, leptons	0
g (gluon)	Strong	Quarks	0
γ (photon)	Electromagnetic	Charged leptons, quarks	0
H (Higgs)	Weak	Massive fermions	0

of the final state, in accordance with the conservation of energy and momentum. Elementary particle decays are also subjected to some other rules of conservation, such as for example the conservation of the number of leptons. An example of a decay into lighter particles is shown in equation (1.1). Although the final state contains three leptons, the presence of an antiparticle ($\overline{\nu}_{\mathrm{e}}$) compensates for one particle (e^-).

$$\mu^- \to \nu_\mu \mathrm{W}^{-*} \to \nu_\mu \overline{\nu}_{\mathrm{e}} \mathrm{e}^- \tag{1.1}$$

The decay of particles is possible as energy and mass are equivalent. If one were to give light particles enough energy, this process could be reversed, creating mass out of energy. At the Large Electron-Positron Collider (LEP) at CERN [44], two highly energetic beams were used to create heavy, unstable particles. A beam of electrons was circulating in one direction, while a beam of positrons was circulating in the other direction. With each particle carrying an energy of ca. 45 GeV, they were able to create Z-bosons at the intersection points of the two beams [29]. Later increasing the beam energy to 80 GeV enabled the researchers to create and study pairs of W^+ and W^- [28]. These heavy particles are however far too unstable to study directly. Therefore, one has to design a detector around the interaction point to detect their decay products, and from there on out deduce the properties of the original unstable particle.

Up to now, there has been no mention of the mundane protons and neutrons, who make up the nuclei of atoms. This is because currently only elementary particles were discussed. Protons and neutrons are the result of an elusive concept, hidden in the strong interaction: colour confinement. Free quarks, as described in Table 1.1 do not exist. Next to an electromagnetic charge, each quark also carries a colour charge (red, green, or blue) of the strong interaction, which allows them to interact via exchange of gluons. Colour confinement now dictates that free particles should be colour neutral, i.e. ‘white’. This can be achieved by combining a particle and an anti-particle, thus cancelling colour charge with anti-colour charge, which leads to e.g. pions. Alternatively, one may combine all three different colour charges to create a colour neutral particle. This is how protons are formed, by combining two u-quarks with one d-quark. These compound particles, created by putting together quarks with gluons, are called hadrons.

1.2 Interactions with matter

Energetic particles lose energy when moving through everyday matter such as gasses or solids. Charged leptons will interact almost exclusively via the electromagnetic interaction. For hadrons, the strong interaction can also become important. When an energetic hadron collides with matter, one of the constituent quarks can be kicked out of the hadron. But since free quarks can’t exist, this quark is said to ‘hadronise’, creating a whole shower of new hadrons. The density of atomic nuclei is usually much lower than that of the electrons bound to them, so if the hadron carries electrical charge, most of the interactions will still be electromagnetic. The weak interaction will be of importance when trying to detect neutrinos, as this is the only way they can interact with other matter. In all other cases, the weak interaction is usually completely negligible.

A more manifest way of describing these interactions with matter, is seeing them as collisions between individual particles. Individual collisions usually transfer only very little energy, 100 eV or less in 90 % of the cases [16], meaning that they lead to ionisations and excitations in gasses, or collective excitations in the case of more strongly interacting matter such as solids. Ionisations create free electrons and ions, which can be collected using electrical fields. Excitations can lead to emission of visible light or UV photons, which in turn can be detected by photosensitive devices.

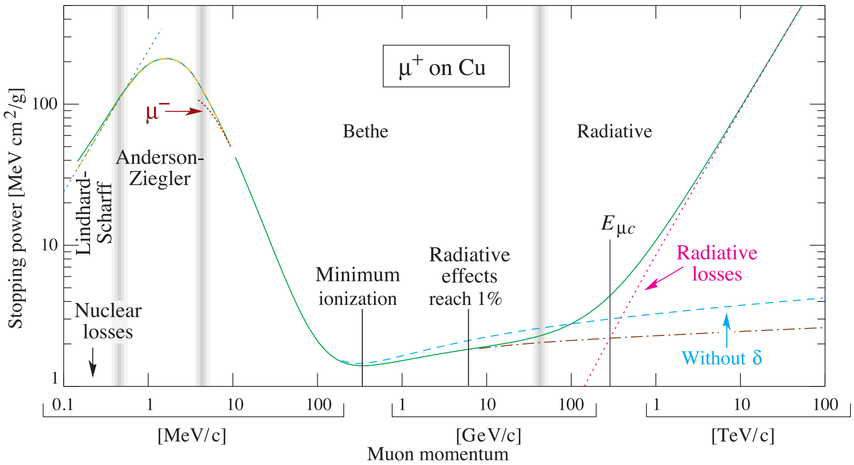

Figure 1.1: Mean stopping power for μ^+ in copper. On the right-hand side, the dotted (magenta) line gives the radiative corrections to the Bethe-Bloch stopping power, indicated by the dot-dashed line (brown). Curves on the left-hand side are derived from experimental data. From roughly 100 MeV to 100 GeV muons can be considered to be mips. [16]

Muons for example, being charged leptons, will loose their energy mainly by interacting with the electrons of the material they move through. The mean energy loss per path length, the so-called *stopping power* $S(E) = \left\langle -\frac{dE}{dx} \right\rangle$, is a property of the entire system, i.e. the material and the impending particle. The material density is usually factored out, since the resulting mass stopping power has only a weak dependence on it. The cited value $S_m = \frac{S}{\rho}$ is then usually given in units of $\mathrm{MeV\,cm^2\,g^{-1}}$.

The mass stopping power for a large energy range is shown in Figure 1.1. For slow moving muons with energies below a few MeV the interactions tend to be very strong. For highly energetic muons, with energies above 100 GeV, radiative losses become important. These radiative corrections account for emission of highly energetic photons and creation of e^+ e^--pairs, amounting to single interaction energy losses of 10^5 eV to 10^6 eV. Between these two extremes, the stopping power can be calculated using the Bethe-Bloch formula. It can be seen that for intermediate energies, the mean energy loss reaches a minimum valley that extends up to the critical energy, above which radiative corrections become important. Within this range of minimal ionisation, the muon is also called a minimum ionising particle (mip), a name that is actually applicable to most relativistic charged particles. The energy at which the radiative corrections become equal in size to the Bethe-Bloch stopping power is denoted by $E_{\mu c}$.

Although Figure 1.1 shows the mass stopping power for copper, the curve doesn't vary too much amongst different materials. The minimum value of S_m is typically found between $1\,\mathrm{MeV\,cm^2\,g^{-1}}$ and $6\,\mathrm{MeV\,cm^2\,g^{-1}}$. This implies that for gasses of atmospheric density, only a few ionisations per mm will occur.

1.3 Collider experiments in high energy physics

As discussed in section 1.1, colliding two highly energetic particles allows physicists to create heavy, unstable particles. Particle accelerators can be typically be divided into two categories: hadron colliders and lepton colliders. The beams of hadron colliders exist of protons, anti-protons or (heavy) ions. By using composite particles, hadron colliders such as the Large Hadron Collider (LHC) [38] turn out to be the perfect 'discovery machines'. The centre of mass energy that is available to create heavy particles covers a broad range of energies, thanks to the energy distribution of the beam particle's constituents. These constituents however also create in a large amount of 'debris' with each collision, resulting in a large background for the experiment. This story is quite different for lepton colliders. Leptons are elementary, point-like particles, so in the case of a symmetric collider the centre of mass energy is simply twice the beam energy, and the background is low. Consequently it is possible to study a large amount of events at a certain energy, but investigating different energies becomes a tedious task. Therefore, lepton colliders are often called 'precision machines' that refine the discoveries made by earlier hadron colliders. Lepton colliders have always been electron-positron colliders like LEP, since these are the only stable charged leptons that exist.

The momentum that is put into the experiment by the accelerator is highly directional, but after a collision, the resulting particles and decay products can essentially travel in any direction. One possible indication of interesting physics, is the presence of a large momentum component p_T, perpendicular to the beam line of the accelerator. A particle with large p_T is the result of a heavy, unstable particle being created at the interaction point. Detecting these decay products allows one to reconstruct the initial particle. To fully define a detected particle, one should measure both its momentum and energy, thus fixing its mass via the well known relation given by equation (1.2a). For particles with large momenta, this can be reduced to equation (1.2b). This simplifies measurements, as the momentum now fixes the total relativistic energy of a particle.

$$E^2 = m^2c^4 + p^2c^2 \qquad \text{(exact)} \tag{1.2a}$$

$$E \approx pc^2 \qquad (pc \gg mc^2) \tag{1.2b}$$

1.3.1 The Compact Muon Solenoid experiment

At LHC, two multi-TeV proton or ion beams are used to create the highest luminosity hadron collider ever built to test the Standard Model around the energy scale of $\mathcal{O}(1\,\text{TeV})$. Thanks to its high luminosity, LHC is well suited to study rare events. The electroweak interaction, and the spontaneous symmetry breaking by the Higgs mechanism, are among the things tested by this experiment. Apart from Standard Model physics, there is also the search for new physics at this high energy scale, that had been out of reach until now for earthbound accelerators. One of the often discussed possible extensions of the Standard Model at high energies is supersymmetry (SUSY), but of course general searches, that are not bound to a single theory, are also performed. The Compact Muon Solenoid (CMS) detector [12] is one of the four major detectors[1] at LHC. Its main focus is studying the proton-proton collisions, for example to detect the Higgs-boson [27], and search for physics beyond the Standard Model.

The CMS detector is a typical modern detector at a (symmetrical) beam collider experiment, and consists of a few concentric parts. Closest to the interaction point, a particle tracker with high spatial resolution can be found, used to determine the momentum of charged particles. This is made possible by the large magnetic field that is created inside the detector, which makes the particles' paths bend according to their momentum. The central tracker thus fixes the energy of the charged component of the event, via equation (1.2b). Next up moving outwards from the centre, is the electromagnetic calorimeter (ECAL). It is designed to fully stop the electrons and photons created by the collision and subsequent decay(s), and measures the full energy of both the charged and neutral electromagnetic component of the event. To measure the energy of the hadronic component, a larger second calorimeter is present, aptly named the hadronic calorimeter (HCAL). The calorimeters determine the energy of the electromagnetically neutral event component, that the central tracker cannot see. Muons with energies up to 100 GeV, being mips, can travel through several metres of solid iron and tend to escape even from the HCAL. Luckily, they are almost the only ones to do so, making the outside layer of the detector the ideal location to place a subsystem for the muons.

Figure 1.2 shows a slice of the CMS detector. Only one quarter of the detector is shown, but it is of course symmetric with respect to[2] $r = 0$ and $z = 0$. The central part of the detector consists of the tracker, the ECAL and HCAL. It is surrounded by the superconducting solenoid, and an extensive muon system interspersed with the iron return yoke. Placing all calorimetry inside the solenoid, makes the design very compact, hence the name Compact Muon Solenoid. To simplify the analysis of events, the detector is subdivided geometrically, not in spherical the coordinates (θ, ϕ), but with (η, ϕ): the pseudorapidity and azimuth angle. Equation (1.3) relates the two systems.

$$\eta = -\ln\left(\tan\left(\frac{\theta}{2}\right)\right) \tag{1.3}$$

The muon system [54] is subdivided into three parts: the barrel region and the two end-caps. The muon barrel (MB) surrounds the solenoid, which in turn contains the calorimeters and tracker. The

[1] There are seven experiments at LHC. ATLAS, CMS, LHCb, and ALICE are located at the intersection points of the beams. TOTEM, LHCf, and MoEDAL are three smaller detector, each located near one of the larger experiments.

[2] (r, ϕ, z) is a set of cylindrical coordinates aligned with the beam axis.

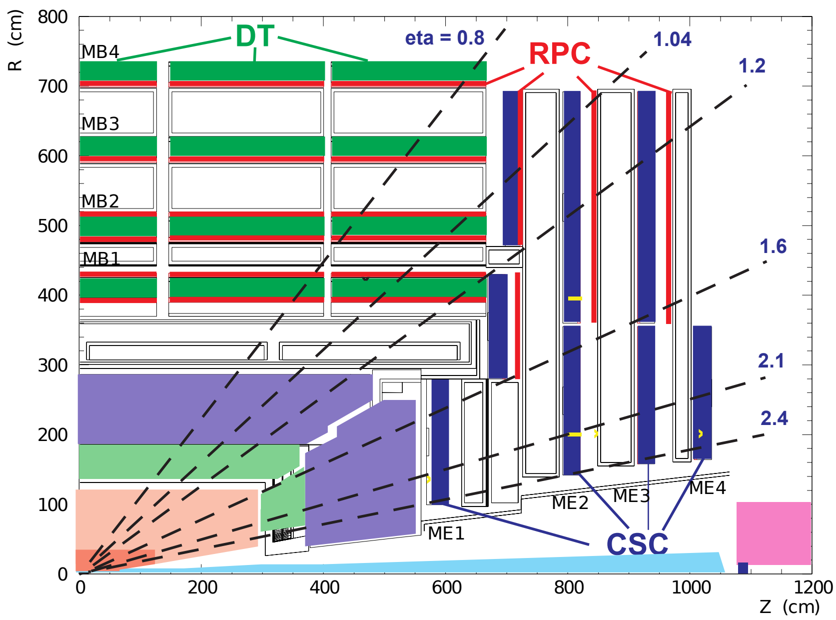

Figure 1.2: Layout of a quarter of the CMS muon system. MB1-4 and ME1-4 indicate the four layers of detectors in respectively the barrel and end-cap regions. The RPCs are indicated in red. The two other subsystems are indicated in green and blue. Respectively indicated in light blue, light green, and light red are the HCAL, ECAL, and central tracker ($r < 3\,\mathrm{m}$ and $z < 5.5\,\mathrm{m}$). [12]

detector is 'sealed of' on both sides by the two muon end-caps (MEs). Tracking of muons is performed by drift tubes (DTs) in the barrel region, and by cathode strip chambers (CSCs) in the end-cap regions, as indicated in Figure 1.2. Triggering on the other hand, is performed by resistive plate chambers (RPCs), which are present in the whole muon system. The First Level (L1) trigger of CMS reduces the $\mathcal{O}(10^8)$ interactions per second by a factor of one thousand, by quickly selecting the events that contain muons with large p_T, using dedicated hardware. The Second Level (L2) trigger, implemented in software, further reduces this event rate to $\mathcal{O}(10^2)$ recorded interactions per second. This huge rate reduction is needed to be able to store the interesting events for later analysis, while discarding the large background of uninteresting events.

During the first long shutdown of the LHC (in 2013 and 2014) the RPC subsystem will see the addition of the fourth layer of end-cap RPCs [57], the construction of which Ghent is contributing to. Current research is also ongoing to increase the detection rate capabilities of the RPCs, for them to be able to handle the increased intensity of radiation after the second long shutdown and upgrade (scheduled for 2018). It is especially important to improve the detector's rate capabilities, to be able to complete the RPC system in the regions of larger pseudorapidity, which will experience even higher rates after the upgrade. It is for this high luminosity upgrade that the RPC described in chapter 5 will be developed.

1.3.2 Calorimeter for linear collider experiments

Always looking into future experiments, physicists are currently contemplating to build a large linear electron-positron collider. Currently the most advanced propopsal is the International Linear Collider (ILC) [20]: a 30 km long device, that would accelerate electrons and positrons up to 500 GeV in its first phase. This will be a precision machine, with one of its goals being the refinement of the discoveries made at LHC. To obtain this high precision data, the events will have to be accurately measured by the detector(s).

The CALICE collaboration aims to design and test several calorimeter concepts for use in ILC detectors [7]. To achieve the required high resolution, most detector concepts employ a particle flow algorithm (PFA). Using a highly granular calorimeter, the shower development can effectively be tracked in all spatial dimensions, which provides the possibility of a more precise energy measurement [55] of the events. Figure 1.3 shows a simulated high resolution measurement in a detector concept for ILC whose layout

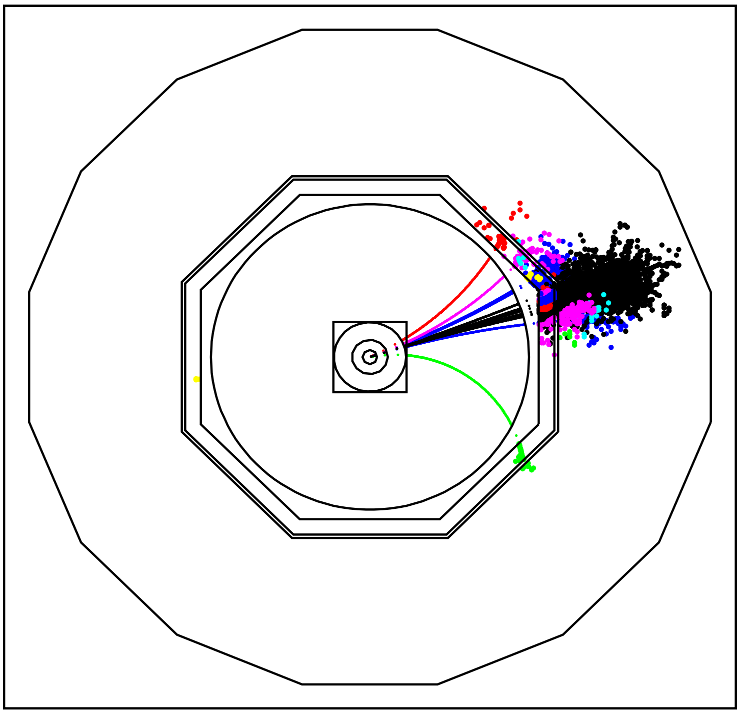

Figure 1.3: Simulated decay of a $Z \rightarrow d\overline{d}$ decay in one of the ILC detector concepts. The full simulated event $e^-e^+ \rightarrow ZZ \rightarrow \nu\overline{\nu}d\overline{d}$ contains two neutrinos that escape undetected, hence the imbalance in measured transverse momentum. The dots in the outer rings indicate the recorded hits in the ECAL and HCAL. [55]

is similar to the layout of the CMS detector. One of the proposed HCALs concepts for ILC employs alternating layers of iron and RPCs, each a few mm thick. The particles then interact and lose energy in the iron layers, while the RPC layers sample the shower as it develops, with a resolution of $\mathcal{O}(1\,\text{cm})$.

Chapter 2

Resistive plate chambers

In 1981 Santonico and Cardarelli [52] presented their version of the localised discharge spark counter developed by Pestov et al. [49] a few years earlier. Both versions of the detector were characterized by a good time resolution of $\mathcal{O}(1\,\mathrm{ns})$. This is comparable to, or even better than, scintillation detectors read out with photomultiplier tubes (PMTs). However, these new types of detector were able to combine this good temporal resolution with a high detection efficiency ($> 95\,\%$) and very large active areas up to a few square metres. All while also maintaining a good spatial resolution of $\mathcal{O}(1\,\mathrm{cm})$. The design by Santonico and Cardarelli, dubbed the 'resistive plate counter', had some important improvements over the slightly older 'localised discharge spark counter'. The semiconductive glass in the original design was replaced by a plastic with similar bulk resistivity ($10^{10}\,\Omega\mathrm{cm}$ to $10^{11}\,\Omega\mathrm{cm}$ instead of $10^{9}\,\Omega\mathrm{cm}$ to $10^{10}\,\Omega\mathrm{cm}$). This plastic, Bakelite, is still used in RPCs since it's a low cost material. Another advantage was that the plastic detector could be operated at atmospheric pressure, instead of 12 times atmospheric pressure. This greatly reduced the risk of gas leaks, thus improving the reliability. Finally, less mechanical precision was required when constructing the detector, once again lowering its total cost. All these improvements that made the detector simple and cheap to construct, and relatively easy in operation, have contributed to its continued popularity in high energy physics.

2.1 Construction and operation principles

2.1.1 Gas gap

The basic component of any RPC is a gap between two parallel plates, filled with a certain gas mixture, as shown in Figure 2.1. Across this gap a high voltage is applied either by grounding one plate and applying a positive or negative high voltage to the other, or applying a high voltage to both plates. When an energetic charged particle passes through the gas volume enclosed by the plates, it ionises the contained gas. This liberates electrons, which are then accelerated inside the gap by the strong electric field. The electrons and ions are not accelerated indefinitely, but collide with the gas molecules, thus losing part

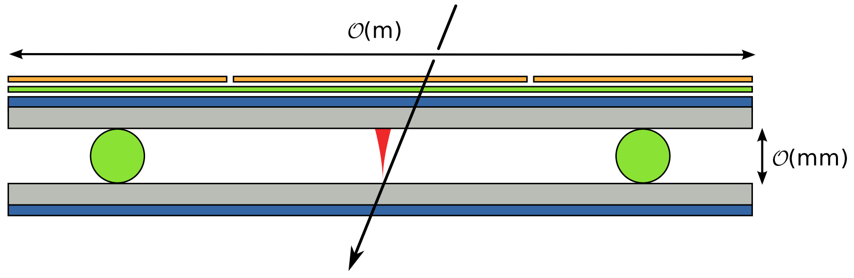

Figure 2.1: Diagram of a RPC showing the different components and typical dimensions. Shown are the resistive plates (grey) with their coating (blue), and gap spacers (green discs). The read-out strips (orange) are positioned next to the gap, at the anode side. An insulating foil (green) provides electrical isolation of the two. A particle that passes through the device (arrow) ionises the gas and creates an avalanche (red).

of their energy. This process of collisions and re-accelerations is called drift, and in doing so clouds of charged particles reach a maximum average velocity, aptly named the drift velocity. The electric field is so strong however, that Townsend multiplication occurs, i.e. on average every colliding electron liberates more electrons and an exponential growth of the number of free electrons occurs. This creation of an avalanche of free electrons is an essential element in detecting a particle by means of a RPC.

Maintaining a uniform electric field across the detector is important since it ensures that the gas amplification is independent of the position of the avalanche. For large area RPCs this requires inserting spacers between the places to maintain a uniform gap width, by preventing them from bending independently. This could happen due to sagging under their own weight, or electrostatic attraction from the high voltage difference. Fishing line, due to its low cost, is often used as spacer material, but a smaller amount of dead space can be achieved by using small discs or balls glued at regular intervals. Usually, the device is operated with a closed volume, so a spacer is also applied around the circumference of the gap to achieve gas tightness.

2.1.2 Signal induction

To understand how the signal is formed in a RPC, let us first have a look at the simpler ionisation chamber. Much like the RPC, the ionisation chamber consists of two parallel plates, which are metallic in this case, separated by a gap of width g. When a particle passes through the chamber, it ionises N_0 gas molecules in between the plates. The electric field in a standard ionisation chamber is rather small, so no Townsend multiplication occurs, but the ions and electrons are attracted by the electrodes and drift towards them. A mirror charge will be created on the anode due to the electrons and ions drifting towards the electrodes. For an infinite signal integration time, the total induced charge on the anode q_{ind}, caused by the drift of the free charges, would be equal in size to the total charge of the liberated electrons if both the electronic and ionic signal components were to be taken into account. This is shown by equation (2.1) [43], where e is the elementary charge, and N_0 the total number of primary ionisations.

$$q_{ind} = N_0 e \tag{2.1}$$

The drift velocity of the ions v^+ is much lower than that of the electrons v^-, so the ion-induced signal has to be omitted to maintain good rate capabilities. The relaxation time $\tau = RC$ of the read-out circuit, should therefore be approximately of the same size as the rise time of the electronic signal component, i.e. $\tau \approx \frac{g}{v^-}$. When taking only the electrons into account, one has to independently consider each of the n_{cl} clusters created by the ionising particle at initial position x_0^j, containing n_0^j electrons. If the cathode is positioned at $x = 0$, and the anode at $x = g$, the individual clusters will behave as equation (2.2a). The total signal is then simply the sum of the individual signals, as given by equation (2.2b).

$$q_{ind}^j = \frac{e}{g} \times n_0^j (g - x_0^j) \tag{2.2a}$$

$$q_{ind} = \sum_{j=1}^{n_{cl}} q_{ind}^j \tag{2.2b}$$

$$N_0 = \sum_{j=1}^{n_{cl}} n_0^j \tag{2.2c}$$

Using metallic plates as electrodes will cause the induced charge to spread across the surface of the detector. When the anode is constructed of a resistive material, this is no longer the case. In a RPC, it will thus be confined to actual location of the avalanche. Any conductive material outside of the anode — placed against it, but not necessarily in electrical contact with it — will then also pick up the induced charge. This enables one to construct a signal read-out mechanism that is distinct from the amplification mechanism as is illustrated by Figure 2.1. Both can thus be developed (almost) independently from one another, and it is easy to replace either of the two parts.

Equation (2.3) gives the induced signal in the read-out plane of a RPC, where η is the (effective) first Townsend coefficient, and M_j takes stochastic variations of the avalanche sizes into account [4]. The presence of the electrode plates is taken into account by including the weighting potential drop ΔV_w, which is approximately equal to one for the single gap discussed here. Note that the cluster that is created furthest away from the anode will produce the largest signal component. It can also be seen that for $\eta \to 0$ equation (2.3) reduces to equation (2.2).

$$q_{ind} = \frac{e}{\eta g} \Delta V_w \sum_{j=1}^{n_{cl}} n_0^j M_j \left[\exp\left(\eta \left(g - x_0^j \right) \right) - 1 \right] \tag{2.3}$$

Employing a highly resistive material as one of the electrodes to ensure avalanche transparency also introduces a problem. The electrical connection to the electrode should be at one the of the edges of the plate, such that the read-out is not obstructed. When the gas inside the gap is ionised, a current will flow through the resistive material. This could result in a significant voltage drop across certain areas of the electrode, thus creating a non-uniform electric field across the gap. A uniform electric field is however essential to the proper operation of a RPC, because the electron multiplication depends on the field strength. Therefore, a material with lower bulk resistivity than the plate material is deposited on top of the electrode, to ensure that the voltage drop across the surface of the electrode is negligible, while still maintaining the charge transparency. This can be seen in Figure 2.1 where the resistive plates are covered by the less resistive coating, and is discussed in more detail in chapter 3.

2.1.3 Gas amplification mode

Depending on the strength of the electric field applied across the gap, the signal will have different characteristics. For fields smaller than the ones commonly used in RPCs, there is no Townsend avalanche. This drift-only regime is the one employed by conventional ionisation chambers and produces only very small signals. They require good preamplifiers as the produced signals consist only of the primary electrons. When entering the electric field regime of the RPCs, the avalanche sizes grow as the high voltage is increased. This is usually called 'avalanche mode operation' and its signals are described by equation (2.3). The distance of the primary clusters from the anode can differ, depending on the where the gas molecules were ionised. This gives a different length along which the exponential Townsend growth can occur, so a very large range of pulses is possible in this intermediate regime. The use of a preamplifier is still necessary for RPCs operated in avalanche mode.

If the electric field is increased even more, the electron avalanches will start to saturate due to space charge effects. In addition to this, inelastic collisions and reattaching electrons can create UV photons, which could start new avalanches. When these processes becomes significant, the induced signals become so strong that the use of a preamplifier is no longer needed. These large signals are called streamers, and accordingly the RPC is said to work in 'streamer mode'. Figure 2.2 shows the transition from avalanche to streamer signals. Note that the transitional regime, from delayed streamers in Figure 2.2b to prompt streamers in Figure 2.2d, cannot be used for precise timing purposes. The time delay has to show very little spread in order to achieve the nanosecond time resolution.

Streamers create a large number of free charges, producing their large signals. The current flowing through the gap increases, so the voltage drop across the resistive material also increases. For a given RPC with fixed external high voltage, the effective high voltage across the gas gap, and thus the electric field, will then drop. This leads to a maximum rate capability, where the current has increased so much, that the internal electric field has become too weak, and the gas amplification is no longer significant enough to provide detectable signals. Consequently the rate capability of RPCs when operated in streamer mode is lower than when operated in avalanche mode. While reintroduction of preamplifiers would then complicate the setup, high rate capabilities are necessary for RPCs to be of use in environments with large particle fluxes such as the LHC experiments.

When operating in streamer mode, the utilised gas should promote production of streamers. However, to prevent the streamers from expanding too much in the lateral directions, a quench gas is needed in the RPC gas mixture. This quench gas absorbs UV photons emitted by the avalanche, without creating new free electrons. When operating in avalanche mode, this quench gas is even more important to achieve streamer free operation.

2.1.4 Material resistivity and ageing effects

A design parameter of major importance is the bulk resistivity ρ of the resistive plates. To show what values of bulk resistivity one needs to construct a RPC, a few materials used in current detectors or R&D are given in Table 2.1. A higher bulk resistivity leads to a longer recharge time of the plates, and as a

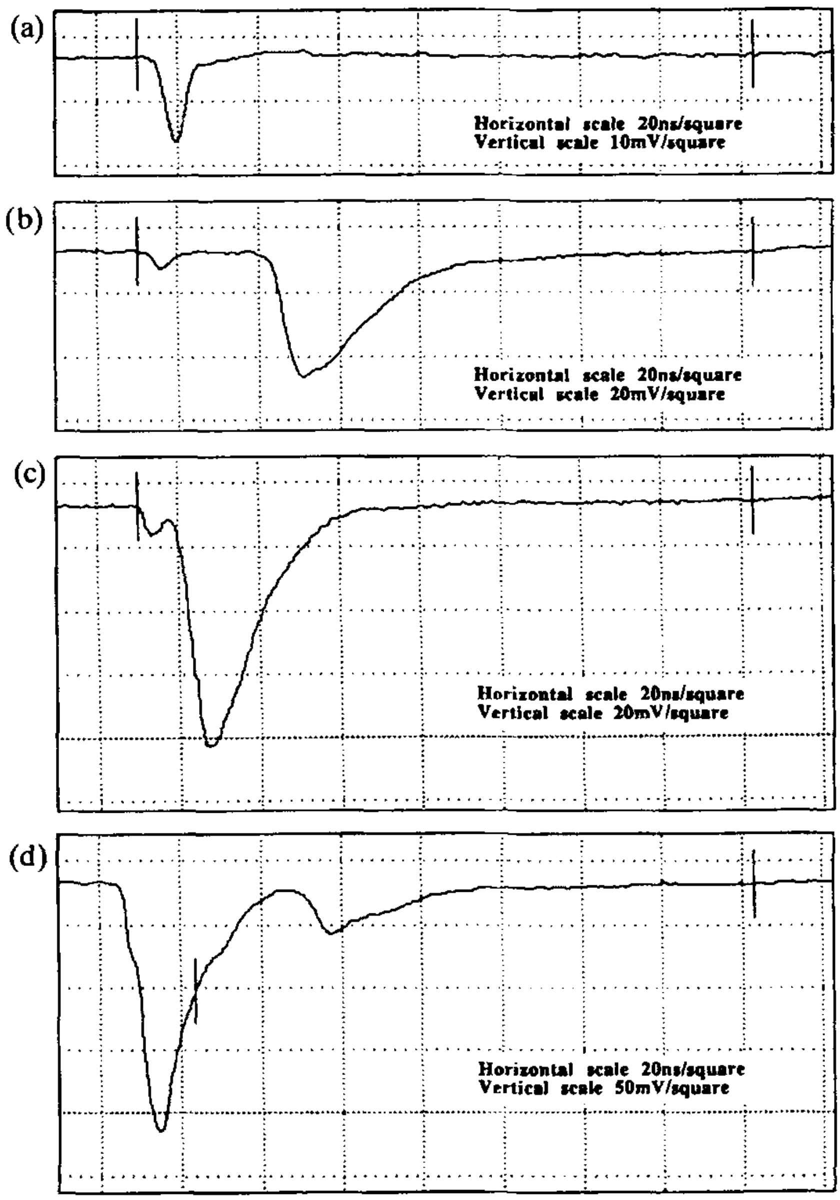

Figure 2.2: Different RPC signals for increasing field strength. Initially only the small and short avalanche signals (a) will be observed. As the field strength increases, larger streamer signals (b) start to appear. Further increasing the field strength will shorten the delay between the two pulses (c) until they eventually merge and even multiple streamers start to appear (d). By Cardarelli et al. [24].

Table 2.1: Typical bulk resistivity values of RPC plate materials.

Material	ρ (Ω cm)
CMS Bakelite [35]	10^9
soda-lime silicate (SLS) glass [14]	10^{12} to 10^{13}
low resistivity silicate (LRS) glass [61]	10^{10}

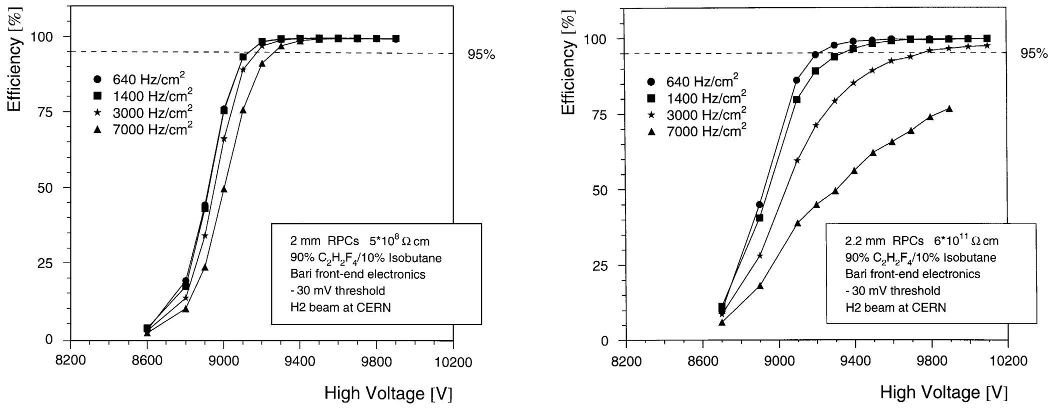

(a) $\rho = 5 \times 10^8\,\Omega\,\mathrm{cm}$ **(b)** $\rho = 6 \times 10^{11}\,\Omega\,\mathrm{cm}$

Figure 2.3: Comparison of detection rate capabilities as a function of resistive plate bulk resistivity for a double gap RPC. The low resistivity material in (a) shows a smaller rate dependence than the high resistivity material in (b). [35]

result the detection rate capabilities drops. Figure 2.3 clearly shows this behaviour. The RPC constructed using low bulk resistivity material (Figure 2.3a) continues to perform well up to $7\,\mathrm{kHz\,cm^{-2}}$, while when using a material with higher bulk resistivity (Figure 2.3b), the performance deteriorates significantly from $3\,\mathrm{kHz\,cm^{-2}}$ on.

Ageing in RPCs is usually characterized by a significant increase in ρ. The highly resistive materials used exhibit a different conduction mechanism than common conductors, such as metals or semiconductors. The latter are electronic in nature, i.e. the moving charges that make up the current a material can carry are electrons[1]. As a current is moving through a material and electrons drift towards the anode, they are resupplied to the material at the anode, cancelling out the loss of electrons. With ionic conduction, this is not the case, as ions cannot easily be resupplied at one electrode, while drifting towards the other. As an example, let us consider the case of SLS glass, more commonly known as float glass. It has been shown that in this common type of glass conduction is due to Na^+ ions [47]. If a high voltage is applied across a piece of SLS glass using two metallic electrodes, the initially uniformly distributed Na^+ ions will diffuse towards the cathode, a process which depletes the glass of its conduction mechanism. Bakelite conduction is also ionic in nature, caused (in part) by H^+ ions originating from water left inside the plastic during polymerisation of the material [59]. This provides a possible solution to reduce the ageing of the Bakelite, namely the addition of water vapour to RPC gas, which prevents depletion of the H^+ ions.

A study has been performed by Morales et al. [46], comparing different materials suitable for use in RPC construction. One of the studied aspects was the ageing due to transferred charge in the materials, as shown in Figure 2.4. To increase ion mobility, the materials were heated to ca. 75 °C. It can be seen that the Bakelite, which was not humidified in this case, ages very rapidly. Due to the increased ion mobility, the values of ρ are lower than during normal RPC operation, but the rise of its value will not disappear as such when operating the material at room temperature. The LRS glass however, appears to exhibit a different conduction mode at elevated temperatures. At lower temperatures, ionic conduction does not appear to be activated, resulting in a lower conductivity, but one that is electronic in nature [60]. Consequently, there is only a small rise in bulk resistivity, even after depositing $1\,\mathrm{C\,cm^{-2}}$. This

[1]Usually, conduction by holes is considered distinct from conduction by electrons, but since the former is just a simplification of the concept of 'absence of an electron', both will be considered as 'electronic' here.

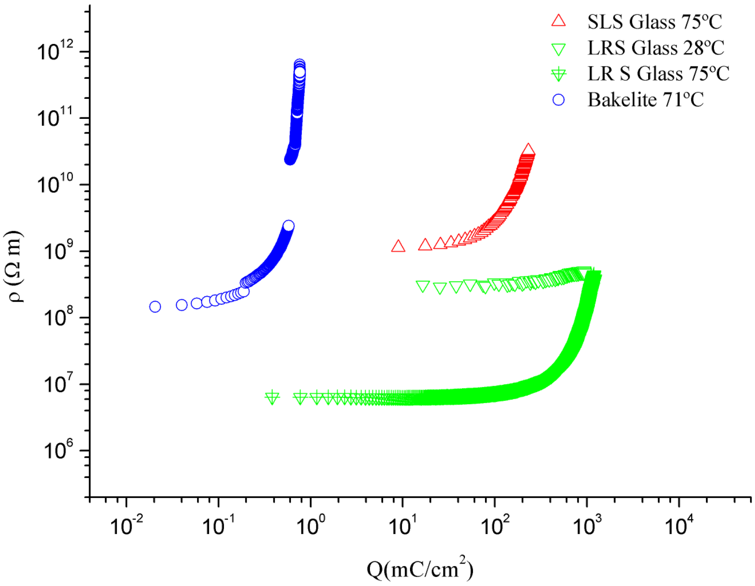

Figure 2.4: Comparison of the bulk resistivity of different resistive plate materials as a function of the total transferred charge. Measurements for LRS glass were performed at two temperatures. [46]

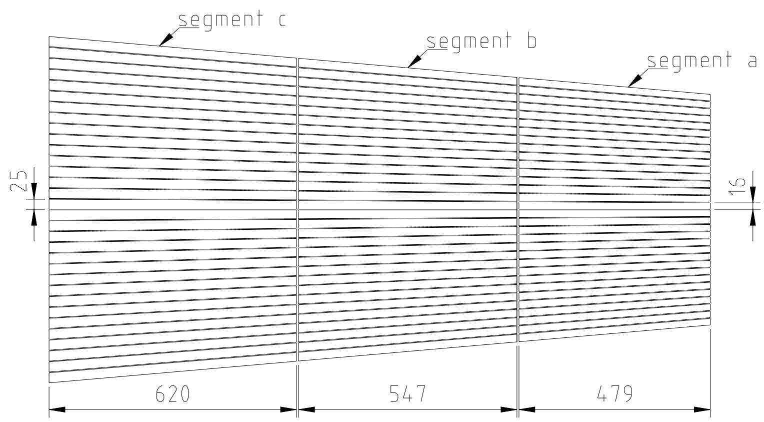

Figure 2.5: Read-out strip pattern of a CMS RE/3/2 chamber. Indicated are the pseudorapidity segment, and strip dimensions in mm. [8]

makes the LRS glass developed at Tsinghua University (China) an ideal candidate for a glass RPC that can withstand extended periods of high rate operation.

2.1.5 Read-out patterns

Acquisition of information happens, as noted in section 2.1.2, by picking up the electrical signal induced by the electron avalanche inside the gap. If a single sheet of conductive material, e.g. copper, were to be placed against the anode, the spatial resolution of the RPC would be as bad as that of an ionisation chamber. The electronic avalanche is however localised inside the gap to an area of a $\mathcal{O}(10\,\mathrm{mm}^2)$. Consequently one can split up the read-out plane in several strips or pads with dimensions of $\mathcal{O}(\mathrm{cm})$, to keep the number of strips firing at the same time reasonably close to unity. Figure 2.5 shows a typical strip pattern used by CMS, divided into three pseudorapidity segments (see also section 2.4.1).

Due to the fast rise-time of the signals, long strips behave as transmission lines. Impedance matching is thus required to avoid signal reflections. The first RPC detector by Santonico and Cardarelli used copper strips, 3 cm wide and placed 2 mm apart, to have an impedance of 50 Ω. This value matches the one commonly used in electronics for signal processing.

The number of pads or strips is usually limited by the electronics used to read out the signals from the conductive surfaces. Pads are thus often avoided due to the large number of read-out channels required to gather all the signal information, although advancements in circuit integration have greatly improved possibilities. Alternatively, perpendicular strip patterns could be used at the anode and cathode side of the RPC, from which one can then deduce the hit position in the plane of the detector. High resolution read-outs have also been developed more recently [26], but these require more advanced electronics to calculate the hit position due to the large number of strips or pads firing simultaneously when a particle passes through the RPC.

2.2 Detection efficiency curves

The mip detection efficiency of a RPC depends on the gas multiplication, as described in section 2.1.2. Of the two relevant parameters, the effective Townsend coefficient η and the gap width g, the former depends on a number of parameters. The largest dependence comes from the electrical field inside the gap. This is determined by the applied high voltage and the uniformity of g, as a smaller gap width implies a stronger field for constant high voltage. The density of the gas mixture is also a relevant factor, which in turn depends on the ambient temperature and pressure.

The gap width variation is fixed during manufacturing and will not change during operation. To ensure stable operation of the RPC, one should thus correct for the change in gas density, which can be achieved using the effective high voltage HV_{eff}. Given the ambient pressure P and gas temperature T, the applied high voltage HV can be corrected to HV_{eff} using equation (2.4) [31]. This is then the voltage that would have to be applied to achieve the same gas multiplication if the ambient pressure and gas temperature were P_0 and T_0 respectively. Equation (2.4) can also be used the other way around, to calculate the HV to be applied in order to maintain constant HV_{eff}.

$$HV_{\mathit{eff}} = HV \times \frac{P_0}{P}\frac{T}{T_0} \tag{2.4}$$

The detection efficiency ϵ, defined as the ratio of number of detected particles and the number of incident particles, shows a characteristic evolution. For small values of HV_{eff}, the efficiency is zero. Starting from a certain threshold, ϵ rises to a plateau athigh efficiency. The steepness of this efficiency rise, and the maximum value depend on the construction of the RPC (see also section 2.3). When increasing HV after reaching the efficiency plateau, at some point the detection efficiency will start dropping again. The point at which streamers appear, depends on the gas mixture and the gap width [34, 62].

The start of the efficiency plateau can be fitted with a sigmoid function, given by equation (2.5), describing the shape of the curves in Figure 2.3a. This function has an asymptotic value ϵ_{max} that gives the value of the maximum efficiency plateau. The point where ϵ reaches 95 % of ϵ_{max} is given by HV_{knee}, and indicates where the plateau starts. λ is related to the slope of the curve at the inflection point, where half the maximum efficiency is reached at HV_{50}.

$$\epsilon = \frac{\epsilon_{max}}{1 + e^{-\lambda(HV_{\mathit{eff}} - HV_{50})}} \tag{2.5}$$

The difference in high voltage between HV_{knee} and the point where ϵ starts dropping of again is the width of the plateau, and determines the tolerance one can maintain when constructing a RPC. Take for a example a plateau width of 400 V around a central value of 10 kV, then this gives one a maximum deviation of 200 V if the high voltage is set to the middle of the plateau. For a nominal gap width of 2 mm, this implies that the tolerance in g is only 40 µm, which is a very stringent design restriction.

2.3 Multi-gap resistive plate chambers

Section 2.1 discussed signal formation for a single gap in avalanche mode, as shown in Figure 2.1 and Figure 2.6a. Detection efficiency can be improved by combining multiple gaps, thus adding the individual signals in the read-out. The simplest approach is to take two single gap layers with the anode sides facing towards each other, and placing the read-out strips in between as shown in Figure 2.6b. A more advanced way of achieving a multi-gap structure, is by starting from a single gap with read-out on one side, and inserting additional thin resistive plates between the outer electrodes. Figure 2.6c for example, shows a

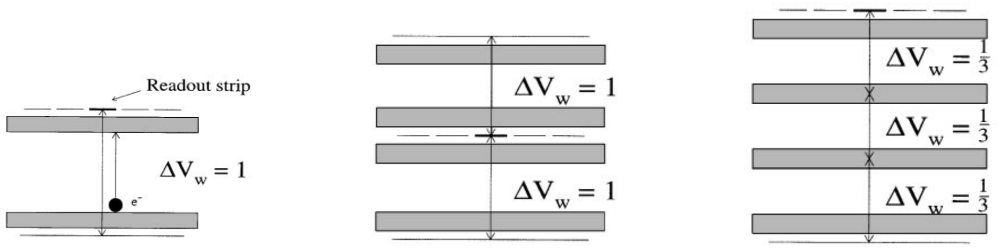

(a) Single gap **(b)** Double gap **(c)** Multi gap

Figure 2.6: Comparison of different gap configurations. [4]

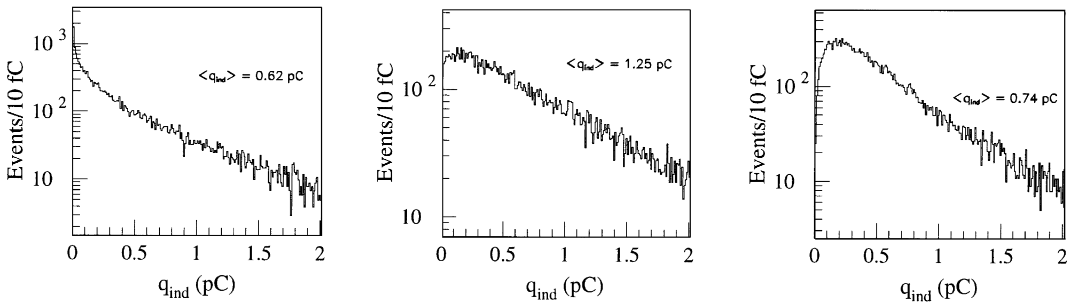

(a) Single gap **(b)** Double gap **(c)** Multi gap

Figure 2.7: Simulated charge spectra of the different gap configurations from Figure 2.6 in avalanche mode. Gap widths are 2 mm and $\eta = 9\,\mathrm{mm}^{-1}$. [4]

triple gap structure. In this case the total thickness of the detector is not significantly altered and η is still the same as in the single gap.

The detection efficiency improvement in the double gap structure has two causes. Firstly, by adding the signals of two independent gaps, the mean induced charge is effectively doubled. This means that the same detection efficiency could be reached at lower electric field values, so with smaller probabilities of streamer signals. The second cause lies with the spectrum of the induced charges. For a single gap this follows the power law behaviour visible in Figure 2.7a, so it has a non-vanishing value for $q_{ind} \to 0$. The read-out has a non-zero detection threshold, so a certain fraction of the induced signals will never be detected. By combining two gaps, the spectra are convoluted and the resulting spectrum no longer diverges for small signals, resulting in a larger fraction of detected avalanches, and thus a potentially higher value of the maximum detection efficiency. Figure 2.7c shows that this effect is even more pronounced for multi-gap RPCs.

2.4 Resistive plate chamber implementations

2.4.1 The Compact Muon Solenoid muon system end-caps

At CMS, the RPCs and read-out strips follow the (η, ϕ) coordinate system described in section 1.3.1. In the muon system end-cap design, there are four layers with each three concentric rings [54]. Using this geometrical layout each type of RPC chamber has its own number RE/M/N, which indicates that its placed in the end-cap, on the Nth ring of the Mth station, counting outwards from the $z = 0$ plane and beam axis. The barrel region has an analogue naming scheme. The RE/*/1 chambers cover a section of $\Delta\phi = 20°$ and contain four pseudorapidity segments in the case of RE/1/1, or two otherwise. The RE/*/2 and RE/*/3 chambers cover a section of $\Delta\phi = 10°$ and contain three pseudorapidity segments. Although ideally all substations should be divided into the pseudorapidity segments as indicated in Figure 1.2, the RE/(3,4)/2 and RE/(3,4)/3 substations have same geometry as the RE/2/2 and RE/2/3 substations respectively, to simplify construction.

The read-out strips of the end-cap RPCs of CMS are trapezoidally shaped, to follow the detector geometry. Each strip covers 5/16° and runs across one pseudorapidity segment, so a fully equipped

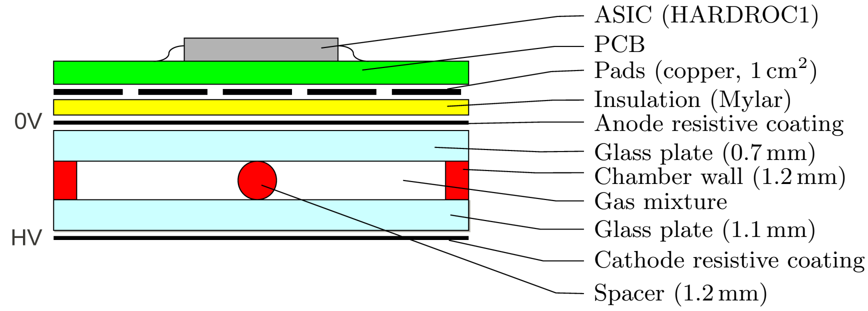

Figure 2.8: Schematic cross section of the CALICE glass RPC. [14]

detector has a total of more than 3×10^5 strips per end-cap [8, 54]. As an example, the strips of an RE/3/2 chamber are shown in Figure 2.5. Read-out of the strips is performed by an application-specific integrated circuit (ASIC) [3]. A more detailed discussion on the CMS RPC front-end electronics can be found in chapter 4.

The chambers consist of a double gap structure, with resistive plates made of low resistivity Bakelite and a gas gap of 2 mm [35]. The read-out strips are positioned between the gaps, as shown in Figure 2.6b. The used gas consists of 95.2 % $C_2H_2F_4$ (R-134a), 4.5 % iC_4H_{10} (isobutane), and 0.3 % SF_6, and is kept at 21 °C [31]. This mixture has an effective first Townsend coefficient $\eta = 8.3\,\mathrm{mm}^{-1}$ at the operating high voltage of ca. 9 kV, ensuring an avalanche amplification regime as simulated by Abbrescia et al. [4]. $C_2H_2F_4$ is a environmentally acceptable freon, and has good timing characteristics [48]. The isobutane and SF_6 are needed to quench the rate reducing streamer signals [23, 62]. The SF_6 does a particularly good job at this, ensuring a wide maximum efficiency plateau [23]. The gas is humidified for 35 % to 40 %, in order to stabilize the Bakelite resistivity, as described in section 2.1.4.

2.4.2 Sampling calorimetry for future linear colliders

As explained in section 1.3.2, a highly segmented read-out is required by the CALICE Collaboration RPCs to implement the particle flow algorithm. This is achieved by using a grid of copper read-out pads of $(1 \times 1)\,\mathrm{cm}^2$ [14]. These pads are also read out using a custom ASIC [14, 22], which is power-pulsed, i.e. only powered during read-out, to reduce the power requirements of the detector.

The resistive material that will be used is float glass. Due to its production procedure[2], the glass sheets are flat, have a very uniform thickness, and a smooth surface. This reduces the intrinsic noise of the gap, without having to be treated with linseed oil like Bakelite [2]. As shown in Figure 2.8, the anode glass sheet is thinner than the cathode (0.7 mm vs. 1.1 mm). This is to be able to place the pads closer to the actual avalanche and reduce pad multiplicity at the anode side, while maintaining more structural strength at the cathode. The gap width of 1.2 mm is maintained across the detector with ball spacers.

These RPCs will also be operated in avalanche mode, so it should come as no surprise that the gas mixture is very similar to the one used by CMS: 93 % $C_2H_2F_4$, 5 % iC_4H_{10}, and 2 % SF_6. Note that in this case the gas will not be humidified. During RPC operation, F^- ions are very likely to be produced. These could then react with any water vapour present inside the gap, producing HF. Since the water vapour is not needed to maintain stable RPC operation, and HF is very corrosive with respect to glass, care should be taken to keep the gas as 'dry' as possible.

[2]Float glass is produced, as the name implies, by pouring molten glass onto a bath of tin. The glass is less dense than the metal and will thus float as it is cooled down to create glass sheets.

Chapter 3

Resistive coating

The application and characterisation of the resistive coating mentioned in section 2.1 was the first problem encountered during the preparations for the glass resistive plate chamber (gRPC) prototype construction. It turns out that there is no standard procedure for applying the coating, which leads to the question of what characteristics a proper coating of a RPC should have. Using the available silk screen tools and paint available, a coating procedure was determined that should ensure that future gRPCs constructed in Ghent can maintain constant properties across different production batches.

3.1 Properties

The single most important parameter to characterise the resistive coating, is the *sheet resisitance* R_S. Imagine a rectangular sheet of a material with bulk resistivity ρ and thickness t. The resistance of this sheet, with dimensions L and W, is then given by equation (3.1). It can be seen that R_S must have the same units as R, since $\frac{L}{W}$ is dimensionless. This makes sense, as the resistance of the sheet does not depend on the absolute dimensions of the sheet, but only on its shape. To avoid confusion, the unit of R_S is usually denoted as $\Omega/\Box$, i.e. 'resistance per square' or 'resistance per unit surface'.

$$R = \frac{\rho}{t} \times \frac{L}{W} \equiv R_S \times \frac{L}{W} \tag{3.1}$$

The resistive coating of a RPC has to ensure that the gap can recharge after an event and provide a uniform electric field, without shielding the read-out strips too much from the charges moving inside the gap [11]. As discussed section 2.1, using a conductive electrode coating would lead to a spreading of the induced charge and thus loss of spatial resolution. In this way, the coating can have its influence on the cluster size, i.e. the number of read-out strips that fire simultaneously. This spreading is only significant up to a certain value of the sheet resistance of the coating, as for growing sheet resistances, the cluster size will decrease up to some intrinsic minimum value. This lower bound is due to the finite transversal size of the avalanche when it reaches the cathode. An estimate can be made of the minimal cluster size, for a disc shaped avalanche footprint with radius r, strip pitch p, and strip separation s. If no spacing is assumed between the strips, then the strip width $(p - s)$ is just the strip pitch. Supposing that the signal cluster size will be 1 when the avalanche overlaps with a single strip, and 2 when it's on the edges of two adjacent strips, the mean cluster size N_{str} is given by equation (3.2). This is the average of the cluster size, weighted with the respective strip surface fraction where this cluster size can occur. For example, with a strip pitch of 15 mm, an avalanche spot size of 10 mm^2, and 2 mm strip separation, N_{str} equals 1.1. In addition to spreading by the resistive coating, cross talk between the strips can also increase the mean cluster size. An intense background of neutrons and gamma rays as with the LHC experiments will also contribute to the observed mean cluster size, since they can trigger avalanches much like any other particle.

$$N_{str} = \frac{2r + (p - s)}{p} \tag{3.2}$$

For high sheet resistances, one may run into different problems. A too high value of R_S would prevent the electric field from being uniform enough to achieve an equal detection efficiency across the

Table 3.1: Resistive coating sheet resistance values of a few selected experiments.

Experiment	R_S	Material
Santonico and Cardarelli [52]	$1\,\mathrm{M}\Omega/\square$	Conductive paper
CMS [54]	$300\,\mathrm{k}\Omega/\square$	Graphite paint
HARP [18]	$200\,\mathrm{k}\Omega/\square$	Graphite tape
CALICE [7]	0.5–$2\,\mathrm{M}\Omega/\square$	Graphite paint

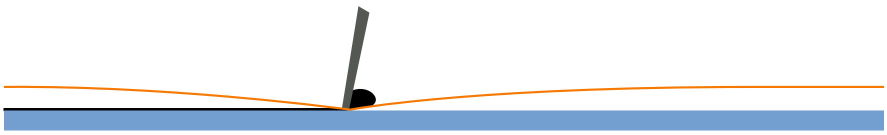

Figure 3.1: An illustration of silk screen printing, showing how the ink is forced through the screen, onto the substrate.

gap. Typically, the sheet resistance is chosen to be at, or slightly above, the value that ensures minimal cluster size, which is around $1\,\mathrm{M}\Omega/\square$. Values for RPCs used in a few selected experiments are shown in Table 3.1.

In any reasonable electrical application, glass or Bakelite would be considered insulators, and the electrode coating a resistive material. Now however, one depends on the small current the resistive plates of a RPC can conduct, so the coating could be considered 'conductive', as its resistivity is much lower. Here however, considering that the conductivity is low for both the coating, as well as the plates, they will both be referred to as 'resistive'.

3.2 Silk screen printing

To apply a resistive coating to the RPC plates, one can employ a few different techniques. Santonico and Cardarelli [52] for example, used conductive paper as the 'coating' of their first RPC. A frequently used method nowadays, and also the one used here, is silk screen printing.

With silk screen printing, a fine mesh of wires (the screen) is positioned above the substrate on which one wishes to deposit a layer of paint. In this case, the substrates are glass plates, and the paint will make up the resistive coating. An amount of paint is deposited on the screen — not on the substrate itself — along one edge of the substrate. The coating is then applied by pulling the paint across the screen with a suitable (metal) squeegee. As the paint is pulled across the screen, it is forced through the fine mesh and deposited on the substrate that is placed underneath the screen, as illustrated in Figure 3.1. Figure 3.2 demonstrates the action of painting the glass, showing the tools used. After coating, the paint is dried and if needed cured at elevated temperatures.

For the development of our glass RPC prototype, we used a mixture of a conductive (Electrodag 6017SS [5]) and a resistive paint (Electrodag PM-404 [6]). Some properties of these paints may be found

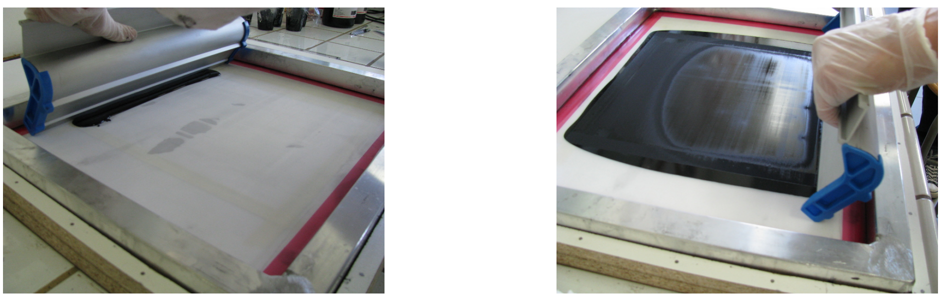

(a) Positioning the squeegee **(b)** Pulling the paint across

Figure 3.2: A physicist in the act of applying resistive paint via silk screen printing. The glass onto which the paint is deposited is underneath the screen and not visible in this picture.

Table 3.2: Paint properties provided by the manufacturer. [5, 6]

Paint	Type	R_S (25 µm dry coating thickness)	Curing
Electrodag PM-404	resistive	$R_S^r > 1\,\mathrm{G}\Omega/\square$	At least 5 min at 120 °C
Electrodag 6017SS	conductive	$R_S^c = 35\,\Omega/\square$	

Table 3.3: Properties of the silk screen.

Dimensions	Thread density	Thread type
34 cm × 50 cm	62 threads/cm	Monofilament polyester

in Table 3.2. The conductive paint consist of conducting carbon particles, dispersed in a non-conducting thermoplastic resin. This thermoplastic resin is also what makes up the resistive paint. By mixing the two paints, in theory one can obtain any intermediate value of R_S by diluting the concentration of carbon particles. After deposition, the paint is cured for 10 min at more than 120 °C, and the glass is left to slowly cool down during at least 30 min. This is to prevent sudden temperature changes that might fracture the glass sheet.

The coating thickness only depends on the density of the wires in the screen and the viscosity of the paint, so silk screen printing allows one to apply uniform layers of a controllable thickness. Preferably, as shown in Figure 3.1, the screen is positioned floating above the substrate. It then only touches the substrate when the squeegee passes over, which should improve layer thickness uniformity. Some properties of the used screen are given in Table 3.3.

Possibly also a mask is used, to prevent certain areas from being coated. This mask can be an emulsion applied to the screen to create a stencil, i.e. to clog the mesh so that paint cannot pass through. Alternatively, the mask can be placed in between the screen and the resistive plate, e.g. by using tape to cover the edges of the substrate as shown in Figure 3.3a. The tape masking approach does have the added complication that the tape introduces an extra layer that could prevent proper deposition of paint close to the mask. The added tape thickness might not allow the screen to touch the substrate when applying paint. When using paper masking tape, which is fairly thick, the paint had to be pulled across two to three times in order to achieve a coat with satisfactory coverage. This was solved by using a much thinner electrical tape. Having to deposit paint only once should also ensure that the coating thickness is more uniform across the painted surface, and that the desired sheet resistance value is actually reached. When depositing multiple layers, the sheet resistance will drop due to increasing coating thickness. At this point, we did not yet employ a screen floating above the glass. The central part of the screen was thus already saturated with paint, while more and more paint was forced through the mesh close to the tape. Indeed, the decrease in R_S was most noticeable around the edges of the coating, close to the paper masking tape.

(a) Applying the mask

(b) Resulting (wet) coat

Figure 3.3: Masking the glass plate with tape to achieve a partially coated surface. Here paper masking tape is shown to be used, which was later replaced by a thinner electrical tape.

(a) Top view **(b)** Bottom side

Figure 3.4: The CRP used to measure the sheet resistances. Also visible with the red and black plastic caps is the adapter from BNC to banana plugs, which are more commonly used for basic electrical measurements. Pictures by Vermason.

3.3 Sheet resistance determination

3.3.1 Resistance probe

Measuring a sheet resistance requires a more elaborate approach than other resistance measurements. Instead of measuring the electrical resistance between two points along a one dimensional path, one now needs to determine the resistance experienced by a current taking all possible paths across a surface. This can be achieved by using a concentric ring probe (CRP)[1] which complies to the IEC 61340-2-3 standard. The probe consists of two concentric, ring-shaped, conductive pads visible in Figure 3.4b, between which one measure a resistance. Using the conversion factor of $10\,\square^{-1}$ provided by the manufacturer, the measured resistance can be converted to a sheet resistance. It has to be noted that when applying force, a better contact between the surface and the CRP can be achieved, thus lowering the measured resistance. For this reason, the probe is loaded with a certain mass, as described by the standard mentioned above. When the probe is placed on top of a flat and level surface, the same force will be applied for all measurements, thus ensuring reproducibility.

The internal resistance R_{CRP} of the probe, given by equation (3.3), can be determined by placing it on a sheet of polished copper, the resistance of which can be neglected. This internal resistance should subsequently be subtracted from all measurements performed with the CRP, but is negligible for all but the most conductive paints.

$$R_{CRP} = (8 \pm 1)\,\Omega \tag{3.3}$$

Values for R_S of around $1\,\mathrm{M\Omega}/\square$ will give a resistance of $100\,\mathrm{k\Omega}$ when measured with the CRP. Table 3.2 shows that the sheet resistance values can span a very large range of values across eight orders of magnitude. The lower part is within the range of the multimeter used for these measurements. Since the input impedance of the multimeter in DC mode is more than $10\,\mathrm{M\Omega}$, the current flowing through the multimeter will be negligible and will not contribute to the measured current, when determining 'small' resistance values. This is no longer the case for values of $R \gtrsim 10\,\mathrm{M\Omega}$, where a non-negligible part of the current will flow through the voltmeter. Therefore it is advisable to use the Wheatstone bridge described in section 3.3.3 to measure these large resistances. Anything above $5 \times 10^8\,\Omega/\square$ however, requires using a Wheatstone brigde with a large reference resistor, as described in section 3.3.3. At the other extreme, very small resistance values might be influenced by resistances of the cables and connectors, so a four wire measurement could be necessary, which is described in section 3.3.2.

[1]model 222002 by Vermason

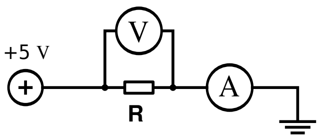

(a) Four wire circuit

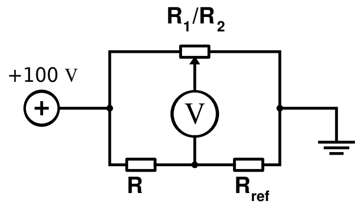

(b) Wheatstone bridge.

Figure 3.5: The two circuits used to measure the sheet resistances, in addition to simple measurements using only the multimeter.

3.3.2 Small resistance values

If one wants to perform a measurement of a resistance, without having to correct for resistances in wires and contacts, usually a four wire circuit can be constructed. Figure 3.5a shows a basic scheme of this kind of setup. Two wires are used for the voltage probe and these are placed at the points between which one wishes to measure the resistance. With the CRP it is not possible to do this, as one cannot place the voltage probes on the sheet surface, so the measured resistance is always the one of the sheet and the CRP. The other two wires connect the voltage source and ampere meter to the CRP. Using the measured voltage V, and measured current I, the total resistance is given by Ohm's law in equation (3.4). R_S can then be found simply by subtracting R_{CRP}. An input voltage of 5 V is used for the small resistances so that I does not grow too large, which may heat up the components and influence the measurement.

$$R = \left(\frac{R_S}{10\,\square^{-1}} + R_{CRP} \right) = \frac{V}{I} \tag{3.4}$$

3.3.3 Large resistance values

The Wheatstone bridge relies on the basic concept of the resistive voltage divider. Take two resistors R_1 and R_2 which are placed in series, apply a voltage V to R_1 and connect R_2 to ground. The voltage V' between the first and the second resistor is then given by equation (3.5). Figure 3.5b indicates that a Wheatstone bridge has two of these voltage dividers. The first consists of the CRP placed on the resistive coating (R) and a reference resistor R_{ref}. The second divider is a potentiometer, so that by adjusting it one can arbitrarily chose the values of R_1 and R_2, of course under the restriction that $R_1 + R_2$ equals the total resistance of the potentiometer. While monitoring the voltage difference between the two dividers, the potentiometer has to be adjusted until there is no voltage difference between the midpoints of the two voltage dividers. At this point, the ratios of the resistance values of both dividers is given by equation (3.6). Because there is no voltage difference, no current can flow from one divider to the other, ensuring that the internal resistance of the multimeter is of no importance at this point. Alternatively, one could also measure the current flowing from one divider to the other. Equation (3.6) is then valid when no current is flowing between the two voltage dividers.

$$V' = V \times \frac{R_1}{R_1 + R_2} \tag{3.5}$$

$$\frac{R}{R_{ref}} = \frac{R_1}{R_2} \tag{3.6}$$

This circuit was only used to determine the sheet resistance of the purely resistive paint coating. Preferably, R_{ref} is at most one order of magnitude different from R. Therefore we used the largest (single component) resistor available at the department with a value of $(10 \pm 0.1)\,\mathrm{G\Omega}$. The potentiometer had a total resistance of $(100 \pm 10)\,\mathrm{k\Omega}$ so that R_1 and R_2 could still be correctly measured using the multimeter. Figure 3.5b also shows that a test voltage of 100 V was used. Although when using a voltage meter as a bridge theoretically any source voltage would do, this higher voltage was used to ensure that enough current would flow to achieve a reliable measurement.

3.4 Paint mixing

Section 3.2 states that any value between R_S^c and R_S^r can be obtained by mixing the the two paints. While this is true in theory, in practice some values are more easily obtained than others. The manufacturer explicitly notes that the paints can be used to achieve sheet resistances from $50\,\Omega/\square$ up to $3800\,\Omega/\square$ at a coating thickness of 25 µm. Note that this is well below the wanted value of about $1\,\mathrm{M}\Omega/\square$.

In the range specified by the manufacturer, the sheet resistance of the mixed paint can be (approximately) calculated using equation (3.7), where f_c is the mass fraction of the conductive paint.

$$f_c = \frac{m_c}{m_c + m_r} \tag{3.7a}$$

$$\log R_S = f_c \log R_S^c + (1 - f_c) \log R_S^r \tag{3.7b}$$

For higher values of R_S — or equivalently small values of f_c — equation (3.7) is no longer valid, as the mixed paint approaches a 'phase transition' from conductive to resistive. This can be modelled using a percolation model, as is done by Kirkpatrick [42] and reviewed by Coutts [33]. Within this model, the resistive coating can be seen as a square grid, with each site either randomly conductive or non-conductive. The probability that any given site is conductive, is then related to f_c. As the concentration of carbon particles drops, i.e. the number of conductive sites, the number of ways to conduct a current across the coating also decreases, thus increasing the sheet resistance. When the critical value of f_c is reached, the chance of finding a conductive path across the grid goes to zero, and R_S is characterised by a sharp increase. This is the point where the mixture goes from conductive to resistive. Mathematically this is formulated as a power law, given by equation (3.8). For all values below the critical value, R_S is equal to the value of the non-conductive paint. In reality of course, the power law would only be approximate around f_0 and R_S does not become infinite, but continuously reaches R_S^r. Additionally, as is characteristic for phase transitions, the fluctuations on R_S would likely become large around f_0. Achieving the R_S predicted by equation (3.8) would then not only get more difficult, but the resulting coating might not have a very stable sheet resistance, even if one has very precise scales available to determine the masses of the two paints.

$$R_S = \begin{cases} R_0 (f_c - f_0)^{-\beta} & (f_c > f_0) \\ R_S^r & (f_c < f_0) \end{cases} \tag{3.8}$$

In order to actually confirm this predicted behaviour of an increasingly rapid growth of R_S as the critical value of f_c is approached, we require measurements of more paint ratios. This is outside of the scope of this thesis however, but from Figure 3.6 one can see that this model at least somewhat describes the measured values. The four fitted parameters may be found in equation (3.9). Although f_0 agrees with the literature values of 0.1 to 0.2, β can be see to be twice 1.35, the value reported by Coutts [33]. The reason for this discrepancy is not immediately clear.

$$R_S^r = (6.3 \pm 1.3)\,\mathrm{G}\Omega/\square \tag{3.9a}$$

$$R_0 = (61 \pm 35)\,\Omega/\square \tag{3.9b}$$

$$f_0 = 0.14 \pm 0.01 \tag{3.9c}$$

$$\beta = 2.7 \pm 0.4 \tag{3.9d}$$

Figure 3.6 also shows that in order to obtain the high sheet resistance of $1\,\mathrm{M}\Omega/\square$, one needs to work in the critical region of R_S, at $f_c \approx 0.17$. Consequently, knowing the actual value of f_c is of major importance to be able to produce different batches of coatings with equal values of R_S.

3.5 Prototype coating

For our glass RPC prototype we used 1.1 mm thick float glass of $(30 \times 30)\,\mathrm{cm}^2$ (see chapter 5). To ensure that the screen does not stick to the substrate when depositing paint, the screen has to be floating above the substrate. The distance between the screen and the substrate should be sufficiently large so that

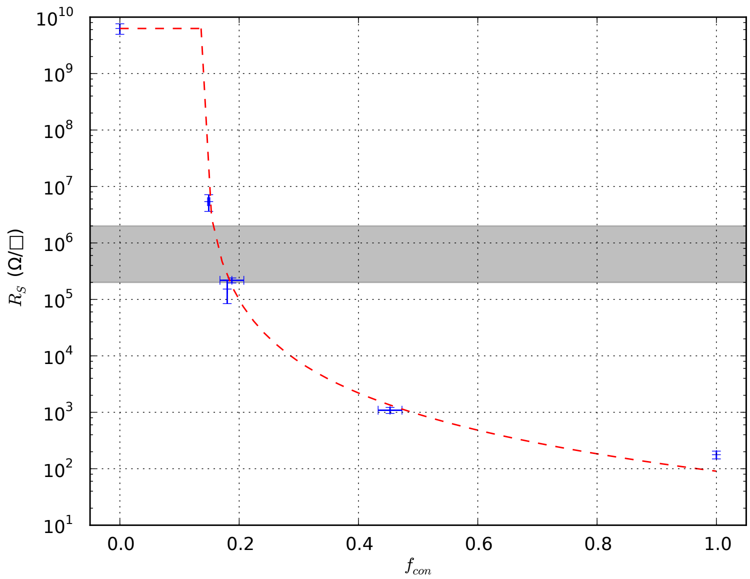

Figure 3.6: Sheet resistance values of several paint mixtures, indicated by the mass fraction of conductive paint. The dashed line is a fit of equation (3.8), to shown the evolution of R_S. The range of commonly used values of R_S is indicated by the grey band (see Table 3.1).

the screen will retract by itself due to the tension that is created by pushing the screen down with the squeegee. For a 1.1 mm thick glass substrate, we ended up using spacers for the screen of ca. 5 mm thick[2], resulting in ca. 3.9 mm of space between the screen and the glass sheets. By applying enough downward force to the squeegee, we were thus able to deposit a fully covering coating in one go. As we did not want to coat the edges of the glass sheets, we created a mask with electrical tape.

Using equation (3.8) with the fitted parameters from equation (3.9), one can calculate that in order to obtain a sheet resistance of $1\,\mathrm{M}\Omega/\square$, f_c has to be 0.167. Taking into account that the resistive paint is less viscous than the conductive paint, a slightly thicker coating could be deposited using the resistive paint. Since this results in a lower sheet resistance, we decided to try and obtain $f_c = 0.16$. The final mass values and conductive mass fraction are given by equation (3.10). According to the manufacturer, approximately $12\,\mathrm{m}^2$ to $14\,\mathrm{m}^2$ can be coated with 1 kg of paint [5, 6]. Some of the paint will also remain on the screen and in the receptacle used for mixing the two components. In order not to run out of paint before finishing the coating, one should add some extra mass to maintain a safety margin. With the total of 70 g of mixed paint it should be possible to coat at least $0.5\,\mathrm{m}^2$. We coated five sheets of $(30 \times 30)\,\mathrm{cm}^2$, of which we ended up using four for the construction of the double gap RPC prototype.

$$m_c = (11.207 \pm 0.001)\,\mathrm{g} \tag{3.10a}$$
$$m_r = (58.834 \pm 0.001)\,\mathrm{g} \tag{3.10b}$$
$$f_c = 0.16 \tag{3.10c}$$

An example of the sheet resistance measurement of one glass plate is shown in Figure 3.7. The indicated numbers are the mean values over the surface covered by the CRP. It can already be seen from this single example that the sheet resistance is not uniform, and that there is a tendency to lower values around the edges of the coating. The full sheet resistance distribution of the batch painted with the mixture from equation (3.10) is given by the histogram in Figure 3.8. The dashed line shows a Gaussian function whose mean and standard deviation are those of the set of measurements of R_S, given by equation (3.11). It can be seen that the real sheet resistance distribution can actually not be described

[2]This is equivalent with stacking two €0.50 coins.

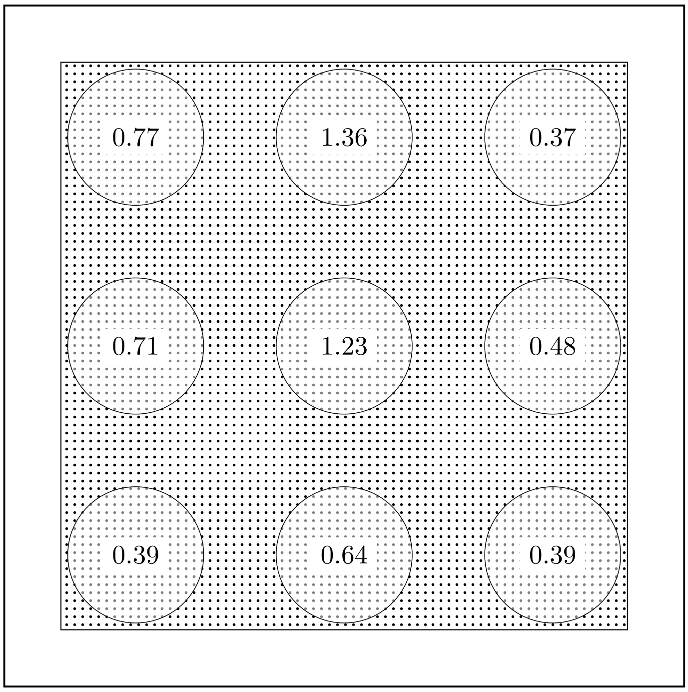

Figure 3.7: Example of sheet resistance measurement using the CRP. The dotted area indicates the part of the glass sheet that is coated. The numbers inscribed in the circles indicate the sheet resistance at that position in MΩ/□.

with a single Gaussian.

$$\overline{R_S} = 0.7\,\mathrm{M}\Omega/\square \tag{3.11a}$$
$$\sigma_{R_S} = 0.4\,\mathrm{M}\Omega/\square \tag{3.11b}$$

The non-Gaussion distribution and the position dependence of R_S indicate that a non-uniform coating thickness is most likely the cause of spread in R_S. The centre of the substrate appears to get a thinner layer of paint than the outside edges. Most likely this is caused by the mask and the size of the screen. As noted before, using tape adds extra spacing between the screen and the glass sheets. This causes a thicker layer of paint to be deposited as the thickness of the tape is of the same order of magnitude as the paint thickness itself, i.e. 10 µm to 20 µm, thus resulting in a smaller R_S. Table 3.3 shows that the screen is only slightly larger than the glass sheets. Additionally, due to the width of the squeegee the screen can only be used in one orientation. The angle at witch the screen detaches from the glass after depositing paint will be much larger at the top of the sheet than at the bottom, possibly contributing to the difference in layer thickness and thus R_S, as shown in Figure 3.7.

Despite the above complications, the resulting coating should still be good to use in our prototype. The values of R_S are at least those of CMS, as show in Table 3.1. If the signal spreading due to the coating conductivity is already close to the minimum at CMS, then the larger R_S values in our coatings should not influence signal characteristics, as transparency only increases for larger sheet resistances.

3.6 Coating procedure and possible improvements

To conclude, a coating procedure can be formulated using the above information. Additionally, a few guidelines for possible future improvements will also be given.

Before coating the glass, one should thoroughly clean and degrease both sides of the glass. This ensures that the paint will be applied to a clean surface, and ensures a quick cleaning is only needed for the inside face when the gRPC gaps will be assembled, thus preventing possible damage to the coatings.

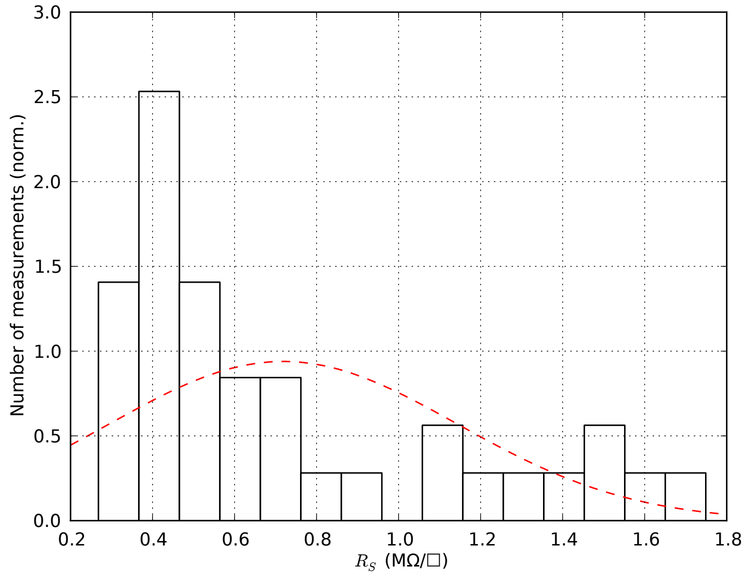

Figure 3.8: Distribution of R_S for a single batch of coatings. The histogram shows the normalised number of measurements, i.e. the sum of the surfaces of the bins is equal to one. A normalised Gaussian using the mean and standard deviation of the data is shown with the dashed line.

Next, the paint mixture is prepared for the desired properties, as described in section 3.4. After weighing the two components of the mixture, they should be thoroughly mixed for several minutes to ensure that the paint is as homogeneous as possible, to prevent variations in the coating properties. Most importantly, variations of the sheet resistance are to be avoided to prevent unwanted signal spreading. First masking the areas one does not wish to coat with a thin tape, as described in section 3.2, one can then proceed by applying the coating. When finished painting, the silk screen and other tools are to be wiped clean and washed with acetone, or a similar solvent [5, 6], to remove remaining the paint.

Once the coating is applied, the paint should be cured as prescribed by the manufacturer at 120 °C or more. After the coating has cured, the glass should be cooled down slowly to prevent fracturing. When cooled down, the glass was wrapped with plastic foil[3] to prevent the plates from getting dirty, and protect the coating during later handling. To ensure a good coating was achieved, it should be characterised as was done in section 3.5.

For substrate masking, one could change to using a stencil by applying an emulsion to the silk screen. This would remove the need of using thin tape to cover the areas that should not be coated, although it introduces the need for a more precise alignment of the glass and the silk screen. On the upside, it would allow for a slightly lower paint usage, as no paint will be lost to coating masks in between the screen and the substrate. The better use of paint will however have to be compared to the extra cost of creating the stencils, many of which might be needed if several different glass shapes are to be coated.

Given the significant spread in sheet resistance found in the prototype coating, it is advisable to look for a larger screen for future coatings, which could ensure more uniform deposition of the paint. Another possibility could be switching to spray painting. This would mean the coating procedure has to be calibrated once again, since this requires the use of a paint thinner. If a good technique is found however, perhaps this could also lead to more uniform coatings, while it is probably also a more convenient way to coat large quantities of glass.

[3]Although one could probably buy industrial foils, we used a common household plastic wrap which was just wide enough to cover the glass.

Chapter 4

Front-end electronics

The RPCs at the CMS experiment are operated in avalanche mode, so they have the advantage of being able to handle higher rates compared to streamer mode. The downside of operating in avalanche mode, is that the gas amplification of the primary ionisation is substantially smaller, requiring an external electronic amplifier. All the electronics required, from reading out the strips, to communicating the obtained signals to the global processing electronics such as the L1 trigger, are referred to as the front-end electronics. When more sensitive front-end electronics are employed, higher detection efficiencies can be reached at smaller electrical field strength, i.e. charge multiplication. Due to the resulting shorter recharge time, additional improvements to the rate capabilities of the RPC can be achieved. Thus, sensitive electronics can help us in constructing a gRPC suit for high rate environments.

4.1 Design

At CMS, the final front-end electronics have been integrated into one ASIC, containing both the amplifier and pulse shaping for digital signal output [3]. A schematic representation of a single strip or channel processing line can be seen in Figure 4.1. Using a preamplifier, the input signal (a small current) is first converted to a voltage. This voltage is then fed into the gain stage for further amplification, together with a dummy input as a reference. This ensures that non-signal DC fluctuations of the preamplifier stage will be balanced out, as these fluctuations will be common to both the real and dummy preamplifier. The gain stage, being a differential amplifier, is insensitive to them and the final amplified output voltage will not change.

The amplifier stage is then AC coupled to a zero-crossing discriminator (ZCD). RPC strip pulses have a large dynamic range, so if a simple threshold discriminator were to be used, the output pulses would display a time walk of of $\mathcal{O}(10\,\text{ns})$. As the RPCs are used for triggering, a good time resolution if required, and this amplitude time walk would thus be an undesirable characteristic. Thanks to the sufficiently constant rise time of the strip pulses, the ZCD ensures that the amplitude time walk is eliminated. Subsequently, the monostable oscillator is triggered by the output pulse from the ZCD. The monostable provides a fixed length pulse of 100 ns. Although this is a rather long pulse, it is necessary to prevent a possible after pulse or noise from the strip from producing a second signal. A shorter output pulse, and thus dead time, would lead to too many fake events. With an expected maximum rate of 400 Hz/strip during data taking in the CMS detector, this gives a dead time of 4 %, which is deemed acceptable. Finally, the driver stage provides the required power to communicate with the read-out via low voltage differential signaling (LVDS).

Together with some other components, two of the above described ASICs are mounted on a front-end board (FEB) [51]. In this way a FEB is equipped to read out (2×16) channels, which corresponds to (half) the number of strips in one pseudorapidity segment, depending on the chamber type. This board can be connected to the read-out strips with coaxial wires, via a small adapter board, and is mounted on the chambers to minimise the distance and possible interference between the signals and the preamplifiers. Once processed, the LVDS pulses are sent over twisted-pair ribbon cables to the L1 trigger electronics. All FEBs of one chamber are furthermore connected to a distribution board that relays low voltage power, and allows configuration of the detection thresholds.

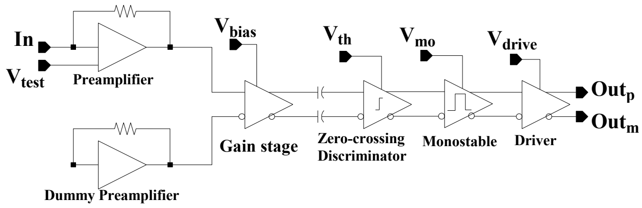

Figure 4.1: Block diagram for signal processing of one strip, as performed by the ASIC. [3]

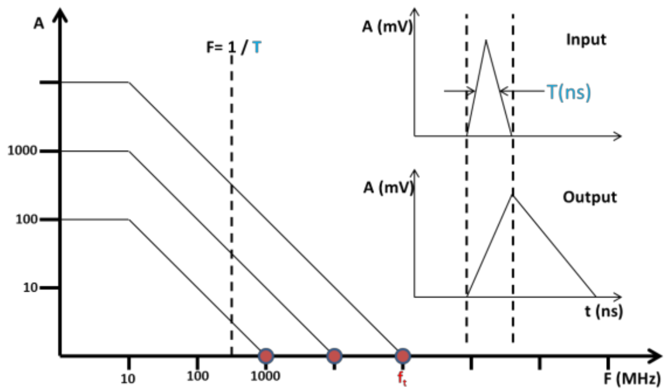

Figure 4.2: Operation strategy of the new preamplifier. [25]

4.2 New preamplifier

Even though the CMS preamplifier is already optimised for low noise [3], recent developments by Angelone et al. [9] have given rise to a new fast charge amplifier (FCA). The goal of the FCA design was to have low noise and be fast, so it could handle signals at high rate. The lower noise level also means that smaller signals can be detected, so the maximum efficiency plateau of the RPC could be reached at lower voltage. This has the advantage of reaching a satisfactory detection efficiency with smaller gas amplification, thus a smaller deposited charge per avalanche. As a result, in a given environment the average lifetime of RPCs is expected to increase. To reach this sensitivity, a strategy as illustrated by Figure 4.2 was employed [25]. The inverse of the signal pulse duration $F = \frac{1}{T}$ is actually beyond the bandwidth of the FCA, but still below the transition frequency f_t of the individual transistors. For frequencies above f_t the transistor gain drops below unity, so it is no longer useful. However, the strip signals themselves can still be amplified, given that the repetition rate is still below the bandwidth of the new preamplifier. The high frequency noise that could potentially mask the signals is now automatically filtered out. Because it is continually present and beyond the bandwidth of the preamplifier, it will no longer be amplified as much as the real signals, thus improving the signal-to-noise ratio.

4.2.1 Experimental setup

In order to test the performance of the new preamplifier, a small board containing electronics for four strips was installed on an spare RE/2/2 RPC chamber from CMS[1]. The preamplifier behaves as a transconductance amplifier, meaning that the output signal is a voltage, proportional to the input current. Further signal processing was then performed by an LRS model 612AL quad discriminator module, that triggers on a preset voltage threshold with a minimal value of 30 mV. This is shown in schematically in Figure 4.3, a picture of the preamplifier board can be found in Figure 4.4a. The discriminator outputs a NIM pulse[2] with a configurable width that was set to 320 ns. Just like in the configuration of the monostable of the CMS electronics, the pulse duration was set to ensure that a single event did not produce two distinct pulses.

[1]The full identifier is RE/2/2-PK044.

[2]Here a NIM pulse, or a transition from a logic 0 to a logic 1 and back, is a 'NIM-Standard Fast Negative Logic Signal'. A logic 1 is defined as a current of -18 mA delivered to a 50 Ω impedance input. [32]

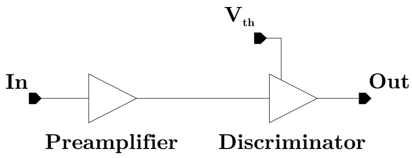

Figure 4.3: Block diagram for signal processing of one strip read out by the new preamplifier.

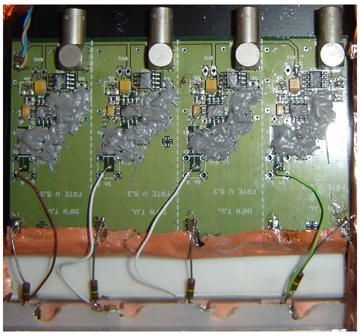

(a) Uncovered

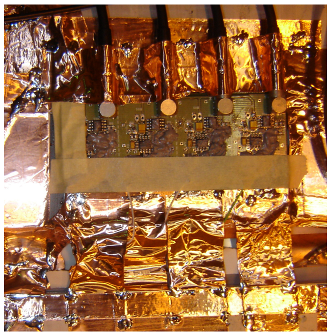

(b) Shielded

Figure 4.4: The board with equipped with the new preamplifier, developed by Angelone et al. [9].

Given that this was only a preliminary test, the board with the new electronics was just provided as a patch on the existing chamber. Special care had to be taken to reduce the level of external noise being picked up by the FCA. This was done in an ad-hoc way, by removing and reattaching unneeded signals cables, grounding cables, and even external devices from common power sockets. To shield the electronics from other sources that we could not control as much, a generous amount of copper tape was applied, as shown in Figure 4.4b. A final element in the noise reduction process, was the use of a filter between the high voltage power supply and the gaps. Inside the metallic enclosure, the read-out strips and gaps should already be well shielded from external sources of noise, so the filter was used to even further reduce the amount of noise picked up by the read-out strips.

The power supply used for the gaps was a CAEN SY 1527. Having a series of independent channels, one was used to power both the top gaps, and a second channel powered the bottom gap. The intermediate filter had eight identical inductive low pass throughputs, and each power supply channel used a chain of three of these throughputs to filter out the high voltage noise.

Using two modules to read out and convert the LVDS signals to NIM pulses, the signals from the CMS electronics obtain the same properties as the shaped pulses from the new preamplifier. This means that from this point on, the same processing chain may be used for a comparative experiment between the new and old preamplifier, thus ruling out any further differences in signal processing.

To perform a detection efficiency measurement as a function of the high voltage supplied to the RPC gaps, we needed an external trigger. This was provided by a pair of scintillators as shown in Figure 4.5, with one directly above, and one directly below the strips that would be read out. The output pulses of the PMTs attached to the scintillators were also shaped using a constant threshold discriminator, similar to the one used for the read-out strips. A schematic representation of the data processing chain is shown in Figure 4.6. The four strips that are between the two trigger scintillators are connected to a fan-in/fan-out. This is a device that has several outputs (fan-out) that provide a NIM logic 1 whenever one of the inputs (fan-in) is a NIM logic 1. To prevent the setup from counting events arising from independent particles in a particle shower, a scintillator is added close to the trigger scintillators that acts as a veto. Another scintillator is positioned further away from the setup, but still powered by the same electronics. It is used as a veto for electronic noise coming from the power supply itself. These two veto signals will inhibit a trigger signal from being produced, even if the bottom and top scintillator signals are in coincidence.

If the noise from the strips were to occur in coincidence with the trigger, an event will be registered, while it is of no physical significance. To be able to count the number of these 'fake events', a dual timer was employed to create a fake trigger. Whenever a real trigger signal is emitted, this trips the delay timer. After about 1 µs, the delay timer starts a second timer that is set such that it mimics, as good

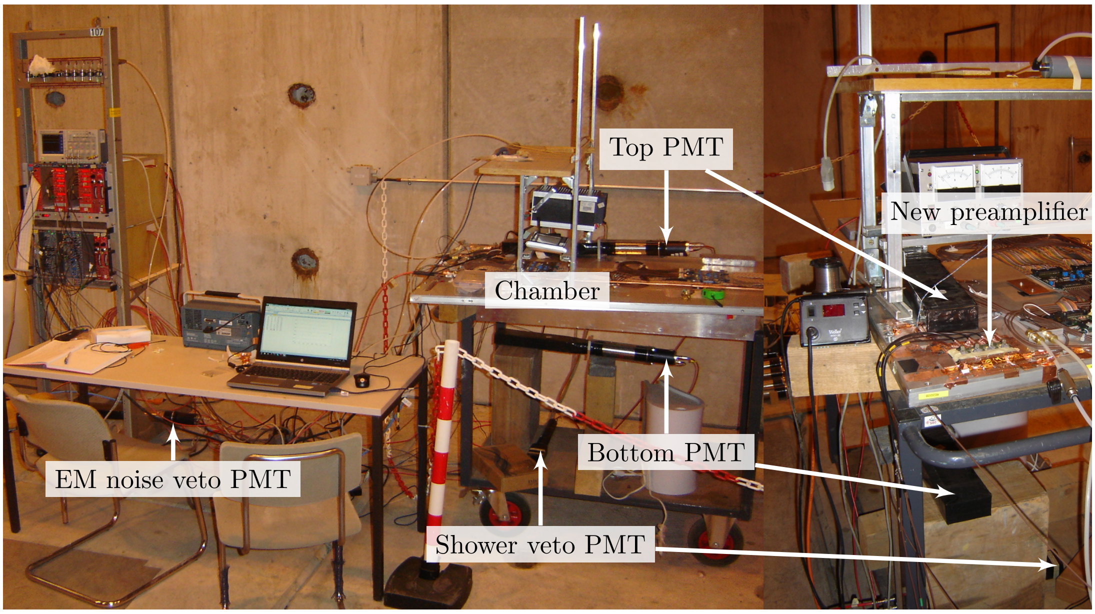

Figure 4.5: Two views of the setup. The different scintillator-PMT packages are indicated, as well as the chamber containing the gaps and read-out strips, and the board with the new preamplifier.

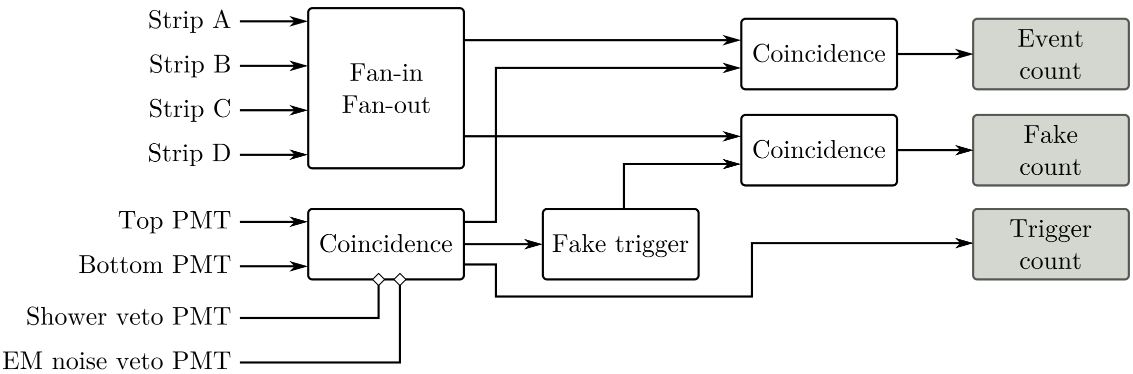

Figure 4.6: Diagram showing the processing of signals from the strips and PMTs (left side). After requiring the necessary coincidences, the resulting pulses are fed into scalers (grey boxes) for counting. Not shown are the scalers that count the rates of the individual inputs.

as possible, the signal from the real trigger. The fake trigger is then checked for coincidence with the fan-out from the strips to give an estimate of the number of fake events that have been registered.

In addition to the counters shown in Figure 4.6, another series of scalers was in use during the experiment. To determine the rates, these scalers counted the number of signals during a 100 s interval for the following inputs:

1. each of the four strips,
2. each of the two trigger scintillators,
3. trigger coincidence,
4. coincidence of trigger and strip fan-out, and
5. coincidence of fake trigger and strip fan-out.

The last three items provide a rough check for the numbers acquired from the three scalers shown in Figure 4.6 and correspond to respectively *Trigger count*, *Event count*, and *Fake count*. For the errors on the counts and calculated efficiency to be reasonably small, at least 300 trigger counts were required, corresponding to approximately 10 min of data taking, per high voltage value.

Finally, to get the timing of the signals right, using an oscilloscope we manually verified coincidence of the trigger signal and fan-out from the strips. By adjusting the window sizes and inserting delay lines, everything was lined up so that even with timing jitter, coincidence of trigger and strip signal would always be detected if it was present.

To be able to provide measurements compatible with previous RPC characterisations by CMS, we used the standard gas mixture of 95.2 % $C_2H_2F_4$ (R134a), 4.5 % iC_4H_{10} (isobutane), and 0.3 % SF_6. Additionally, we strived for a relative humidity of the gas of about 40 %. The relative humidity and temperature of the gas flowing into the chamber were monitored using a Pico Technology HumidiProbe. With each measurement we also took note of some environmental parameters. Using a digital weather station, we monitored the ambient air pressure, temperature and relative humidity. HV is corrected to the effective high voltage HV_{eff} using equation (2.4). The reference pressure $P_0 = 965\,\text{mbar}$ and temperature $T_0 = 293\,\text{K}$ are the values used for the end-caps, so that our efficiency curves can be easily compared.

From the information acquired during the measurements, an estimate of the detection efficiency ϵ can be derived for each value of HV_{eff}. ϵ is obtained by dividing the number of event counts N_e by the number of trigger counts N_t, as shown in equation (4.1a). The error on the efficiency σ_ϵ is directly related to ϵ itself and N_t, and is given by equation (4.1b). For any given N_t, the error acquires it largest value for $\epsilon = 0.5$. Using $N_t \geq 300$, as noted above, the relative error $\frac{\sigma_\epsilon}{\epsilon}$ is at most 6 %.

$$\epsilon = \frac{N_e}{N_t} \tag{4.1a}$$

$$\sigma_\epsilon^2 = \frac{\epsilon(1-\epsilon)}{N_t} \tag{4.1b}$$

A sigmoid function, given by equation (2.5), is fitted to each of the measurements and gives the expected ϵ for a given effective high voltage. The working point HV_{WP} for end-cap RPCs is defined by equation (4.2). By setting the supply voltage for all RPCs at HV_{WP}, it is ensured that they all operate above their individual HV_{knee}, thus compensating for variations between individual chambers.

$$HV_{WP} = HV_{knee} + 150\,\text{V} \tag{4.2}$$

4.2.2 Data processing

As noted in the previous section, signal rates and event counts were acquired using scalers (two CAEN N145 and two CAEN N1145). The resulting number of counts is then displayed on the device and has to be manually entered into a datafile to be available for later processing.

During the experiment, all the monitored variables, rates, and count numbers were entered into a spreadsheet, along with some information about the setup. Later, this information was extracted from the spreadsheet and put into two separate files per measurement run, i.e. per high voltage scan. The first file is a general description file that contains information about the setup during the measurement run. This information is measured at the start of the run and should not change during the course of the high voltage scan. It includes values such as the PMT supply voltages and discriminator threshold, the strip signal thresholds, etc. Other general information such as the chamber type or used electronics is also stored in the description file. To be able to easily process the file contents, the description file is stored using an XML format. The second file contains all the parameters measured per high voltage value as a comma separated values (CSV) list, where the first line of the file contains the column headers, i.e. the names to identify the values in the columns. The CSV file format is widely supported by data processing software, and is in a way a very basic spreadsheet format that is limited to storing a table of data. These file pairs are put in a folder that acts as a kind of database. To have a key to access the data contained in the database, both files need to have the same name, up to the file extension. For example, the data for the measurements using the CMS electronics without HV filter, can be found in the files `cms_unfiltered.xml` and `cms_unfiltered.csv`.

Using Python's built-in libraries and the third party libraries SciPy [41] and Matplotlib [40], a small framework for processing the acquired data was written. The data can be accessed just by using the measurement key, so for the files mentioned in the paragraph above, this would be "`cms_unfiltered`". By making the geometrical information of the gaps, as described by Aftab et al. [8], available to the software, it is able to automatically retrieve the required surface sizes needed to calculate the strip rates and currents per surface unit.

When the software is executed, the data from the CSV files is stored in memory in a 'masked array'. This kind of data container provides a way to tag invalid fields. For example, value that is missing in the data file will be replaced by some default and 'masked out'. Missing values are masked automatically, and one can also manually mask data points. Matplotlib has the advantage of recognizing these masked arrays and will not plot any points tagged as invalid. This provides an easy way of not plotting certain data points, just by masking out the corresponding high voltage value. The plots in the following sections have been produced using this framework, which wraps certain parts of SciPy and Matplotlib to make the process of producing them easier.

Fitting equation (2.5) to the data is also implemented in the code, utilizing the ODRPACK [17] wrapper provided by SciPy. The procedure is implemented with a least squares fitting algorithm, taking only y-errors into account. We thus neglect the errors on HV_{eff}, but since they are small compared to the errors on ϵ, this is not a big problem. Reimplementing the procedure to utilize the full power of ODRPACK, the orthogonal distance regression fitting, would require knowing also the error on HV_{eff}. Although this is currently not implemented and should be straightforward to do so, it is unlikely to give a large improvement of the sigmoid fit. Quick fit convergence can be achieved by supplying the procedure with good initial parameter values. A rough estimate of the sigmoid parameters can be given by equation (4.3). The easiest one is $\langle\epsilon_{max}\rangle_0$, which can just be estimated by taking the maximum of the measured efficiencies. $\langle HV_{50}\rangle_0$ can be estimated by taking the effective high voltage that maximises $E(1-E)$, where E is the measured efficiency normalised to $\langle\epsilon_{max}\rangle_0$. The most elaborate calculation is needed for $\langle\lambda\rangle_0$. After estimating the derivative of the sigmoid at HV_{50}, it is calculated from equation (4.3c).

$$\langle\epsilon_{max}\rangle_0 = \max(\epsilon) \tag{4.3a}$$

$$\langle HV_{50}\rangle_0 = HV_{\mathit{eff}}\big|_{\max(E(1-E))} \tag{4.3b}$$

$$\langle\lambda\rangle_0 = \frac{4}{\langle\epsilon_{max}\rangle_0} \times \left.\frac{\Delta\epsilon}{\Delta HV_{\mathit{eff}}}\right|_{\langle HV_{50}\rangle_0} \tag{4.3c}$$

The code for the framework and the measurement database are available at:
`https://github.ugent.be/sjvheule/rpc-electronics`.

4.2.3 Chamber and electronics characterisation

To ensure that the detection efficiency measurements taken with the above describe setup make sense, the gaps and strip signals were also monitored. This provided two measures of the quality of the gaps and the electronics: the dark current of the gaps and the individual strip rates. These results will then be compared to the properties of the CMS RPCs as reported in literature, before continuing with reporting the actual efficiency measurements.

Figure 4.7 shows the signal rates from the individual strips, coming from the CMS electronics. They show an exponential growth for increasing high voltage, so they must arise from amplification of free charges inside the gap, and not from external noise being picked up by the front-end electronics. The rates also stay well below the upper limit of $10\,\mathrm{Hz\,cm^{-2}}$. Below this value the chance of counting fake coincidences should be very small. In fact, the strip rates per surface unit seen here agree perfectly with the systematic measurements by Abbrescia et al. [1].

The dark currents drawn by the gaps during the measurements are shown in Figure 4.8. Comparing these values of the currents and strip rates to the ones reported by Abbrescia et al. [1], we may conclude that this chamber is suited to perform a representative measurement. The sharp rise seen at the end of the current curves, is most likely due to the gas starting to break down and a non-neglible streamer probability, leading to larger currents [24].

With the new preamplifier the detection threshold V_{thr} could be set lower due to the smaller amount of noise, so it was chosen such that the individual strip rates did not exceed a few 100 Hz. Given that the strip surface in the tested segment is $145\,\mathrm{cm}^2$, this should ensure that the strip rates stay below the above defined limit. For the high voltage scan without noise filter, this required a value of $V_{thr} = 70\,\mathrm{mV}$. After putting the noise filter in place, the threshold could be dropped to the minimum value of 30 mV. In Figure 4.9 the strip rates with the new preamplifier can be seen to be a lot less stable than those of the old electronics: the rates sometimes fluctuate by almost an order of magnitude for a voltage difference

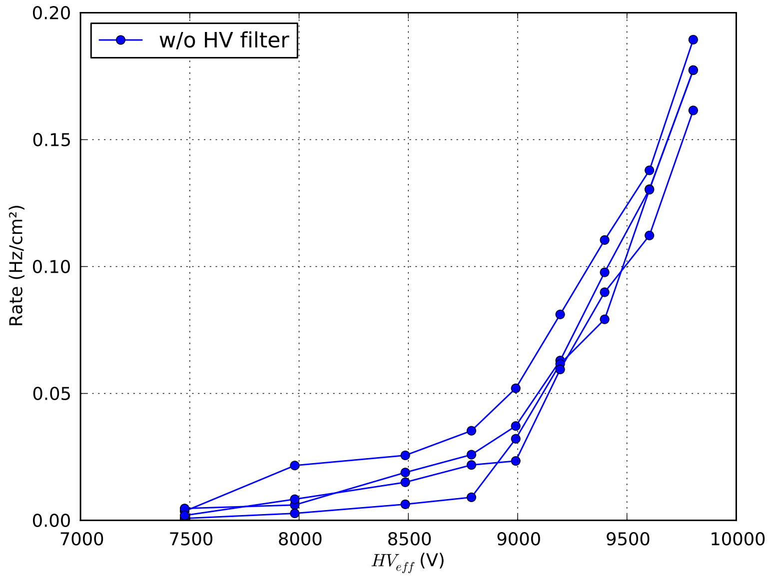

Figure 4.7: Individual signal rates of the strips used in the detection efficiency measurements of the CMS electronics.

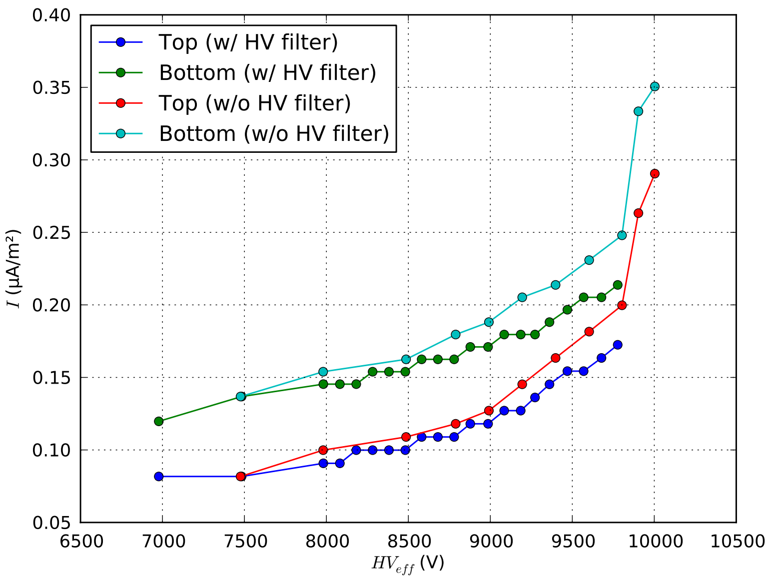

Figure 4.8: Current values reported by the gap high voltage power supply divided by the active surface of the gaps.

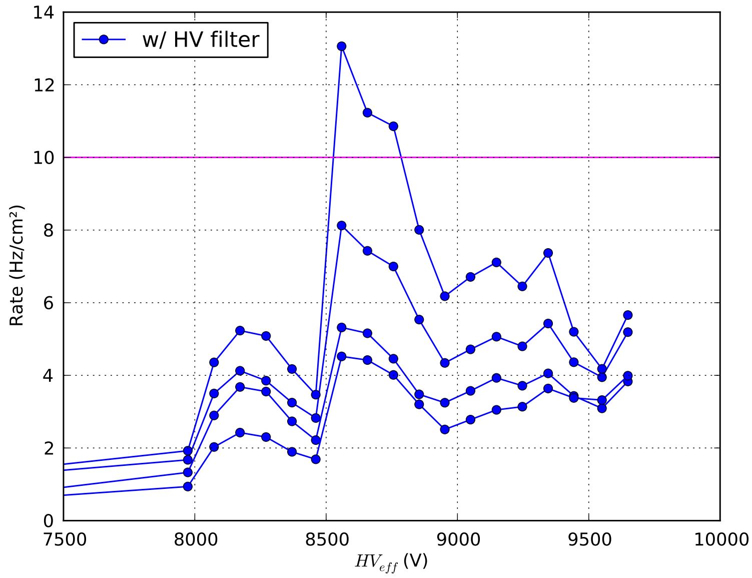

Figure 4.9: Individual signal rates of the strips used in the detection efficiency measurements of the new preamplifier. The magenta line indicates the noise threshold for CMS.

Table 4.1: Fitted parameter values and HV_{WP} for the performed measurements.

	HV filter	ϵ_{max}	HV_{50} (V)	λ (V^{-1})	HV_{WP} (V)
CMS electronics	☐	0.964 ± 0.010	9150 ± 11	0.0126 ± 0.0011	9530 ± 20
	☑	0.976 ± 0.005	9141 ± 5	0.0121 ± 0.0006	9534 ± 13
New preamplifier	☐	0.987 ± 0.005	8724 ± 11	0.0100 ± 0.0007	9170 ± 20
	☑	0.991 ± 0.003	8599 ± 7	0.0090 ± 0.0004	9075 ± 15

of 100 V. Nevertheless with these high strip rates, a trigger rate of 0.5 Hz, and a trigger pulse width of $\mathcal{O}(100\,\text{ns})$, the chance of fake coincidence is still negligible.

After cleaning up the grounding for the power supply of the new preamplifier, the strip rates were remeasured. As it turned out, it was also possible to achieve the same clean, exponential behaviour, despite the more ad-hoc way of shielding and grounding the electronics. Shown in Figure 4.10 are the values measured after the final improvements, as well as the previous values for comparison. One can see that now the strip rates stay below the CMS threshold of $10\,\text{Hz}\,\text{cm}^{-2}$, but are still an order of magnitude larger than the rates from the old front-end electronics.

A rough estimate of the cluster size can be provided by comparing the sum of the four individual strip rates with the total strip rate. Since the total strip rate is just the logic OR of the individual strip signals, this will be lower than the sum of the individual rates, due to strip multiplicity not being equal to one. Figure 4.11 confirms this view. The estimated cluster size $\langle N_{str} \rangle$ is larger than 2 for the lower voltages, and just below 2 for $HV_{eff} > 8.7\,\text{kV}$. Comparing these results with Thyssen [56], the cluster size with the new electronics appears to be above the current cluster size at CMS, which is ca. 1.1 for $HV_{eff} = 9.3\,\text{kV}$. This is likely due to the increased sensitivity of the new preamplifier.

4.2.4 Detection efficiency determination

In Figure 4.12 the efficiency measurements using the CMS electronics are shown. The detection thresholds for the ZCD were set to 215 mV and 220 mV for the measurements with and without high voltage noise filter respectively. These thresholds were chosen to comply with the value of 220 mV used by CMS. Although a slightly higher value of ϵ_{max} was found with the lower threshold, it did not differ significantly from the other value for the old electronics, as can be seen in Table 4.1. The retrieved values of HV_{WP} are

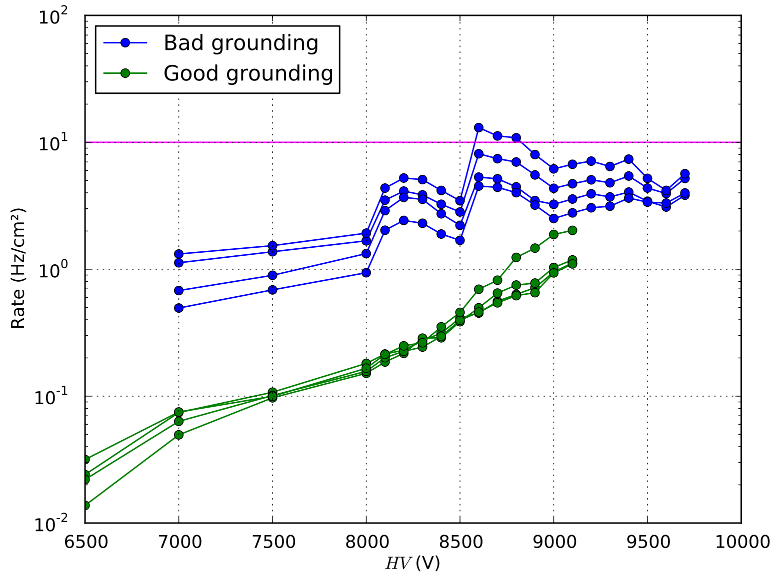

Figure 4.10: Individual signal rates of the strips used in the detection efficiency measurements of the new preamplifier, before and after cleaning up the grounding. The magenta line indicates the noise threshold for CMS.

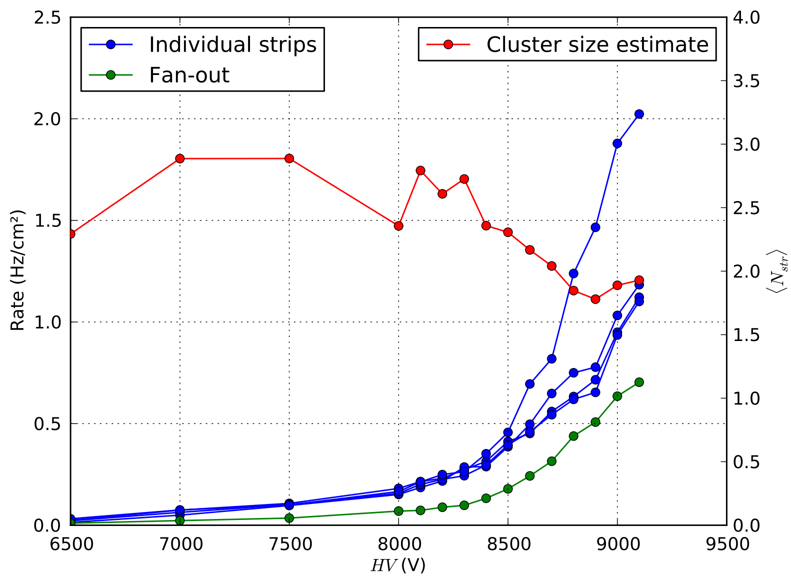

Figure 4.11: Plot of the individual strip rates and total strip rate after cleaning up the grounding for the new preamplifier. Also shown is an estimate of the cluster size.

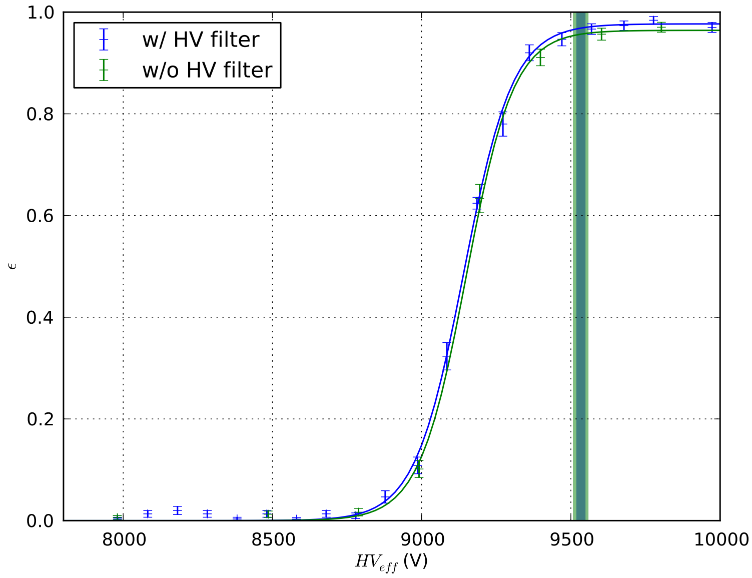

Figure 4.12: Measurement values and sigmoid fit of the efficiency using the CMS front-end electronics.

indicated by the shaded areas in the plots and show the 1σ confidence interval, but also here the results from both measurements are not much different. Overall, the results obtained from these measurements agree perfectly with the results from systematic studies of the RPC chambers reported by Abbrescia et al. [1], confirming that this chamber is well functioning and suited for use in testing the new electronics.

Considering that the threshold on the discriminator was lower when measuring the efficiency with the new preamplifier, one would expect HV_{WP} to shift to a slightly lower value due to more of the smaller avalanches being picked up by the discriminator. In Figure 4.13 and Table 4.1 one can see that this shift to lower HV_{WP} does indeed occur. The efficiency measurements with the new preamplifier were all performed with the shielding seen in Figure 4.4b in place. The ground loop that was eliminated later, resulting in the lower noise rates shown Figure 4.10, was still present when measuring the efficiency curve. Due to the argument mentioned earlier that the chance of fake coincidence is negligible, and the fact that we did not count any (fake) signals in coincidence with the fake trigger, these results should however remain valid.

Figure 4.14 compares the most representative efficiency measurement using the old electronics, with the best measurement for the new preamplifier. For the old electronics, this means no HV filter and a signal threshold of 220 mV. The best measurement, with the lowest HV_{WP}, was achieved for the new preamplifier using the HV filter, and a signal threshold of 30 mV, but without having eliminated the ground loop. This results in a difference in HV_{WP} of (460 ± 30) V, which is a significant improvement. As a result, the gaps themselves will require less power during operation at the working point. One can see in Figure 4.8 that the currents drawn by the gaps drop by 20 % to 30 %. As a result, the drawn power in our preliminary measurement is reduced by $\mathcal{O}(20\,\%)$. This can be calculated using equation (4.4), with (I_0, V_0) denoting the values for the old electronics and (I_1, V_1) the values for the new preamplifier, such that the result is a positive number.

$$\frac{\Delta P}{P} = \frac{I_0 V_0 - I_1 V_1}{I_0 V_0} \qquad (V_0 > V_1) \tag{4.4}$$

Table 4.1 shows that the maximum efficiency is also different, and goes up to 99 %, compared to 97 % when using the old electronics. Abbrescia et al. [4] showed that for the double gap RPC structures used by CMS, there is a non-vanishing fraction of the induced charge for $q_{ind} \to 0$. So for a lower signal threshold, the ϵ_{max} will always increase, irrespective of the applied HV_{eff}, due to a larger fraction of the small avalanches being picked up by the read-out. However, since a different part of the chamber was used for both electronics, this change in ϵ_{max} might just as well arise from a local variation in gap

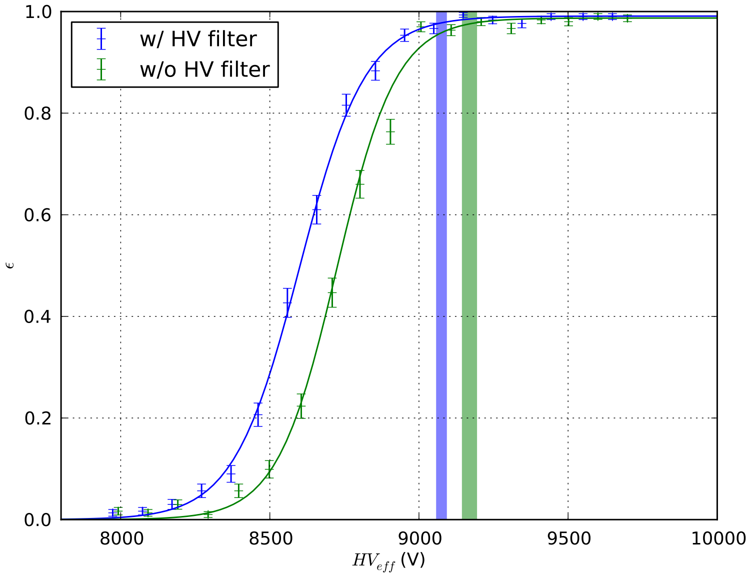

Figure 4.13: Measurement values and sigmoid fit of the efficiency using the new preamplifier.

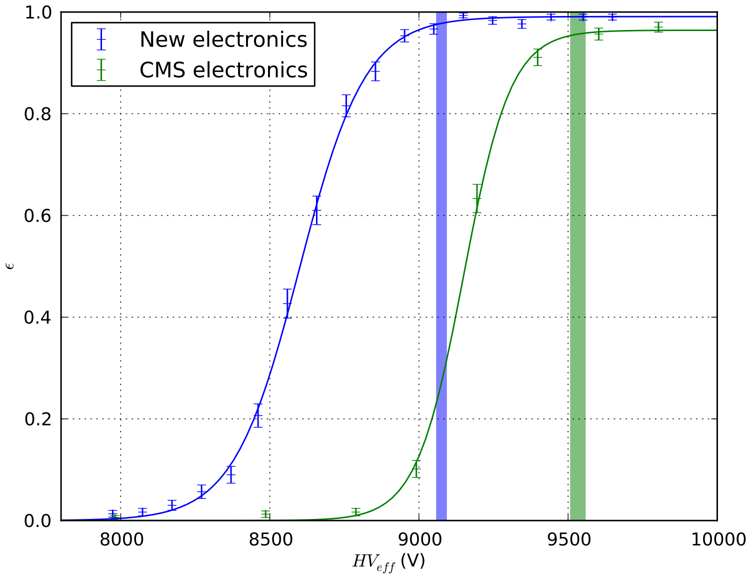

Figure 4.14: Measurement values and sigmoid fit of the efficiency using the new preamplifier and CMS front-end electronics.

performance, so a more elaborate measurement of the maximum efficiency is needed.

4.3 Conclusions and further characterisation

Using a spare chamber from CMS, which we have shown to be well behaving in section 4.2.3, a new preamplifier was tested. Comparing the detection efficiency using the operational CMS electronics configuration, with our best results using the new preamplifier we found an improvement of the working point voltage by $(460 \pm 30)\,\mathrm{V}$. This of course assumes that equation (4.2), used to calculate HV_{WP}, remains (approximately) valid, since it is based on a calibration of the CMS muon system end-caps. Nevertheless, the above result are a good indication that more sensitive electronics can in fact be used to increase the rate capabilities of a future gRPC design for CMS.

It was already noted in section 4.2.3 and section 4.2.4 that the preliminary measurements, however promising, need to be refined. In addition to the high voltage scans performed to determine the efficiency, one should extend these with a scan of the signal detection threshold. Comparing measured signal rates at equal thresholds will provide a more sensible measure of the background, a combination of both the intrinsic gap noise and noise from the electronics. A measurement covering the complete surface of the RPC would also provide a more comprehensive result. Only two times four strips of one pseudorapidity segment were tested, while a chamber of the used type has three such segments of 32 strips each [8]. Equipping more strips, across the whole surface, with the new preamplifier, will give more statistics on several parameters, such as the strips rates, and ϵ_{max}. By testing the new read-out across the complete surface, a comprehensive measurement of the efficiency variations, cluster size, etc. could be performed. Performing an analogous measurement on the same detector with the CMS electronics would allow a thorough comparison of both read-outs.

Alternatively, if at least one segment is fully equipped with preamplifiers of the new type, the cluster size at lower high voltages could be determined. With the smaller gap amplification, the avalanche size will shrink. This could lead to a smaller footprint of the charge deposition on the resistive plates, and possibly smaller cluster size. A reduction of the cluster size also depends on the transparency of the graphite electrodes, as described in chapter 3. If the cluster size arises mainly from the charge smearing by the electrodes, a smaller avalanche footprint can only slightly reduce the cluster size. On the other hand, a lower detection threshold might lead to an increased cluster size due to the smaller induced signal that can be picked up.

Chapter 5

Glass resistive plate chamber prototype

As noted in section 1.3.1, during the LS2 upgrade phase of LHC and its experiments, CMS will have to ensure that its detector will be able to handle the increased radiation intensity in the forward directions once the accelerator comes back online. The current Bakelite RPCs are furthermore not be able to cope with the integrated charge deposited on the plates in the high pseudorapidity regions close to the beam line. Therefore we aim to design a gRPC that does not have this shortcoming. To achieve the highest possible rate capabilities, the idea is the use doped glass develop at Tsinghua University [61]. As shown by Morales et al. [46] and depicted in Figure 2.4, the material shows little ageing even for large integrated charges. It has also been shown that (multi-gap) RPCs constructed with the LRS glass are capable of handling high rates up to at least $9\,\mathrm{kHz\,cm^{-2}}$ [39, 61].

5.1 Full size design

One requires LRS glass for a high rate RPC, but it is currently not possible to produce single sheets of this material large enough to construct a RPC of $(1.2 \times 0.6)\,\mathrm{m}^2$, i.e. the dimensions of an RE/4/1 substation at CMS [8]. It is therefore required that we use smaller pieces of glass, glued together to the required size. The layout for both the top and bottom gap are shown in Figure 5.1. Starting from single glass sheets of $(30 \times 30)\,\mathrm{cm}^2$, the dimensions of the pieces were chosen to minimize the amount of glass cutting required. Attention was also paid to the positioning of the seams, to ensure as little overlap as possible between the two gap layers. Having active area from one of the gaps should at least ensure some detection efficiency. Although the seams will most likely be less than fully efficient, this is preferable over having dead lines across the detector.

Once constructed, the RPC read-out would ideally be based on the new preamplifier, described in

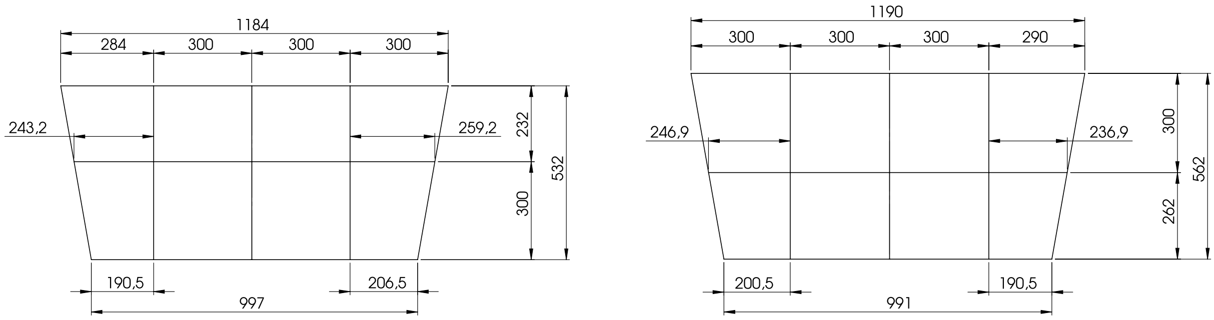

(a) Top gap **(b)** Bottom gap

Figure 5.1: Layout of the individual glass sheets, cut to the correct size and glued together to create an RE/4/1 sized RPC. To allow for the connection to be made between the read-out strips and the front-end electronics, the top gap is slightly shorter than the bottom gap [8]. Dimensions are in mm; drawings by S. Cauwenbergh.

Table 5.1: Inventory of the tools used for glass cutting and cleaning. Article numbers refer to the Bohle catalogue. [19]

Article number	Description
BO 400.0	Carbide glass cutter[1]
BO 02B120	Spare carbide wheels
BO 401.120	Spare turret
BO 032.1	L-square with brace ($80\,\mathrm{cm} \cdot 34\,\mathrm{cm}$)
BO 075	Angle measuring system
BO 5017503	Kevlar cut resistant gloves
BO 5107800	Glass cleaner (1 l bottle)
BO 5107810	Spray head for glass cleaner

chapter 4. This allows the chamber to be operated at lower high voltage, resulting in a smaller charge per detected particle. This reduces the rate at with the integrated charge will grow, resulting in a longer expected lifetime of the gaps.

5.1.1 Glass cutting

Cutting glass is an acquired skill, which requires quite some practice in order not to break or ruin half the sheets one is cutting. Therefore, in order not to waste expensive LRS glass, a first RE/4/1 sized prototype will be constructed using much cheaper float glass. Float glass is available in large sheets, but in order to gain as much experience as possible with constructing a RPC consisting of smaller glass pieces, we will use the same small sheets of $(30 \times 30)\,\mathrm{cm}^2$. A list of tools purchased with Bohle for the glass cutting is given in Table 5.1. All glass pieces have been cut twice according to the layout from Figure 5.1, and are ready to be assembled into plates: two for the bottom gap and two for the top gap.

5.1.2 Glass glueing

To construct the RE/4/1 sized RPC, the glass sheets need to be glued together in an appropriate way to ensure proper operation of the detector. We therefore strived to achieve a thin glue seam, to reduce dead zone, and a flat final surface. If the glass sheets are not lined up with the glue or the adjoining sheet, a sharp ledge will be present. Such distinct surface features are notorious for causing noise and should thus be avoided. This is however a shortcoming that could possibly be fixed by machining the glass after glueing to once again achieve a smooth surface. What machining will not fix, are variations in gap width due to the misalignments. Leading to variations in the electrical field strength, this has an influence on the actual signal amplification, rather than the noise. The tolerance on the gap width depends on the plateau width, as shown by the example in section 2.2.

Several glueing schemes, shown in Figure 5.2, were considered. To provide additional strength to the basic seam from Figure 5.2a, an extra bar of glass could be glued on top of the seam, as shown by Figure 5.2b. The added glass however results in a resistive plate that is thicker at the seams, possibly leading to variations in the read-out. Alternatively an additional spacer could be added according to Figure 5.2c, which might ensure better positioning of the glass sheets. The added width however increases the dead zone, and the gas flow has to be ensured throughout the gap. This could be done by using spacers that do not cover the full length of the seam, or by drilling holes to let the gas flow through.

A few basic initial tests were performed by K. Erpels and A. Fagot, using CAF 4 silicone glue from Bluestar Silicones [21]. This glue has been used before at the HARP experiment [18], where it was also used to glue separate glass pieces to construct a gRPC. The glue has a bulk resistivity of $10^{15}\,\Omega\,\mathrm{cm}$, which is at least 2 orders of magnitude larger than the glass bulk resistivity (see Table 2.1). This high value of ρ implies that the seams will effectively be shorted by the surrounding material, and will not contribute to the active area for any but the lowest rates. Different widths of the seam depicted in Figure 5.2a

[1] The cutting angle of this cutter is 135°, and is suitable for cutting normal glass according to the Bohle catalogue. The spare wheels and turret however have a cutting angle of 120°, and are meant for cutting thin or hard glass. The glass cutter with a 120° cutting angle has article number BO 400.1.

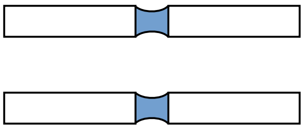

(a) Simple seam

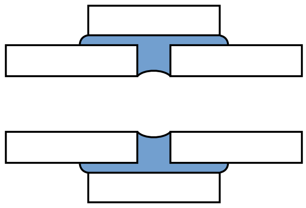

(b) Enforced seam

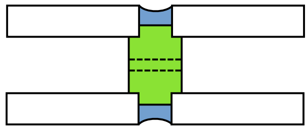

(c) Additional spacer

Figure 5.2: Possible glueing schemes. The rectangles indicate the glass sheets, glue is shown in blue. Shown in (c) in green is an additional spacer.

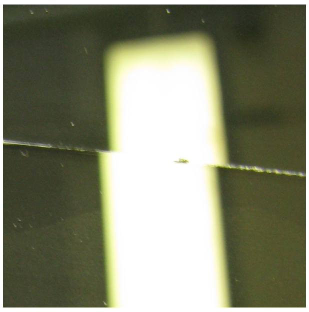

(a) Misaligned plates

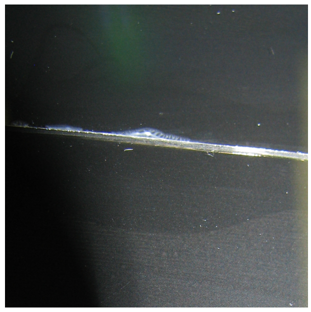

(b) Chipped edges

Figure 5.3: Gas facing sides of painted glass sheets used for glue tests. Surface imperfections such as (a) ledges due to misalignment or (b) chipped edges could lead to higher noise at the seams.

were tested, and a width of $\mathcal{O}(200\,\mu\text{m})$ turned out to be sufficient, even without using a reinforcement as show in Figure 5.2b. Notwithstanding we tried to perform the glueing on a surface plate to try to ensure that the end result would be flat, we were unable to achieve good alignment. This can be seen from Figure 5.3a were the reflections of the two glass pieces don't line up. Even if a good alignment could be achieved, chipped edges as shown in Figure 5.3b could still lead to extra noise.

5.2 Small scale prototype

In order to familiarize ourselves with the construction of a glass RPC, and avoid the complications of composite resistive plates, we decided to construct a small scale, double gap prototype of $(30 \times 30)\,\text{cm}^2$. The design of this prototype is largely based on the CMS chambers, thanks to the availability of RE/4/3 chambers on site due to the contribution of Ghent to the RPC end-cap extension.

By using single sheets of $(30 \times 30)\,\text{cm}^2$ glass, we avoid any effects of glue seams. This allows us to determine the performance of the just gaps, without the possible additional noise. Much like the CALICE RPCs [14], the gap width of the prototype will be 1.2 mm. We will however use 1.1 mm thick glass for both the anode and the cathode. Gas tightness of the gap is achieved by glueing PMMA strips along its circumference, along with custom designed gas inlets (see section 5.2.1). The remaining space between the edge of the glass plates, and the strip spacers will be filled up with electrical grade silicone [36]. Gap width uniformity is ensured by placing four ball spacers[2] at 10 cm separation.

All glueing of the spacers and inlets is done with Araldite 2011 two-component glue [10]. However, since the PMMA spacers are slightly bent they can only be glued to one glass plate at a time to achieve decent positioning. Glue is applied to one side of the strip, which is then applied to the glass, weighted down with a metal bar, and left to cure for at least 24 h. The gas inlet adapters (see below) are glued in together with the spacers, to ensure everything fits and can be glued gas-tight. Two opposing edges of the glass sheet can be done at the same time, resulting in a total glueing time of three days: two days to apply the strips and gas inlet adapters, and a third day to apply the second glass sheet. When glueing on the second glass plate, the inside faces of both plates were cleaned, and any dust was blown of with

[2] Grade 5 ZrO_2 ceramic precision balls from Sceram (10 Chemin des Rosiéristes 69410 Champagne-au-Mont-d'Or, France).

Table 5.2: Electrical properties of materials used in gRPC gap assembly. Values for the gas inlet adapter could not be retrieved, so the given numbers are values which resemble other acrylic plastics, assuming they are similar enough in electrical characteristics.

Material	ρ (Ω cm)	Dielectric strength (kV mm^{-1})
Araldite 2011 [10]	(not provided)[3]	22
Dow Corning 3140 silicone [36]	2.1×10^{14}	15
Strip spacers (PMMA) [15]	10^{17}	19.7
Ball spacers (ZrO_2) [15]	10^{15}	11.4
Gas inlets (acrylic plastic)	(10^{15})	(15)

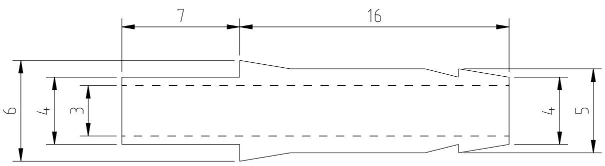

Figure 5.4: CMS RPC gas inlet tube fitting. Dashed lines indicate boundaries of hollow inside. Dimensions are in mm.

compressed air just before closing the gaps. Some electrical properties of the used materials are listed in Table 5.2. The dielectric strength indicates the field strength from which the material starts to break down and loses its insulating properties.

In order to be able to track our glass gaps across different measurements, we devised a naming scheme for the gaps. We chose to go with `GHENT-GRPC-XX-YYY`, where `XX` indicates the gap type series, and `YYY` the gap number within this series. The series number should be identical for all gaps that have the same geometry. The first constructed gap of the $(30 \times 30)\,\text{cm}^2$ prototype thus gets serial number `GHENT-GRPC-01-001`, the second `GHENT-GRPC-01-002`, etc. Complete chambers will be named in the same way, with the series number corresponding to the compatible gaps. The `YYY` part now starts with a 'C' to indicate the serial number corresponds to a chamber, e.g. `GHENT-GRPC-01-C01`.

5.2.1 Gas inlet adapter

Compatibility of the prototype with the existing RPC testing infrastructure used for the RE/4/3 assembly, reduces the amount of work needed to test our gRPC. To be able to connect our gaps directly to the gas system, we decided to design custom gas inlets, which we had 3D printed. Other gaps by e.g. Bedjidian et al. [13] use capillaries with an outer diameter of 1.2 mm, and an inner diameter of 0.8 mm. These capillary PEEK tubes are however very fragile, so require extra care during handling.

The gas inlets of the gaps used for the RE/4/3 chambers consist of two parts. An inlet adapter is glued into the side of the gap together with the edge spacers, to ensure gas can reach the gap volume in a controlled way. A standard tube fitting, shown in Figure 5.4, can then be glued into the adapter. If an inlet were to break during gap testing or chamber construction, the remaining plastic can be drilled out, and the inlet can be replaced.

The first gas inlet we developed for our prototype was a monolithic design, i.e. the spacer and tube fitting would be a single part of plastic as shown in Figure 5.5. The spacer consisted of a 5 mm long insert, was 11.2 mm wide and 1.15 mm thick. The slightly reduced thickness was to allow glue between the insert and the glass plates, while maintaining a final gap width of 1.2 mm. To allow for gas to flow into the gap, a rectangular opening of $(8.2 \times 0.6)\,\text{mm}^2$ was placed centrally on the insert, which has about the same surface area as the opening of the gas tube fitting. The resulting wall thickness of the insert design was thus 0.275 mm. A hollow block between the tube fitting and spacer insert allowed for a smooth transition of both the outside and inside surfaces of the gas inlet, as is shown in Figure 5.5b.

The shape of the inside cavity in this design cannot be formed by single-piece casting, which is why

[3]It has been found that low sheet resistance values of $10^{10}\,\Omega/\square$ can occur when curing the glue in moist air, although we have not experienced any obvious side effects due to this property. By cleaning the surface of the glue when cured with ethanol, one should be able to recover values of $10^{15}\,\Omega/\square$ [53].

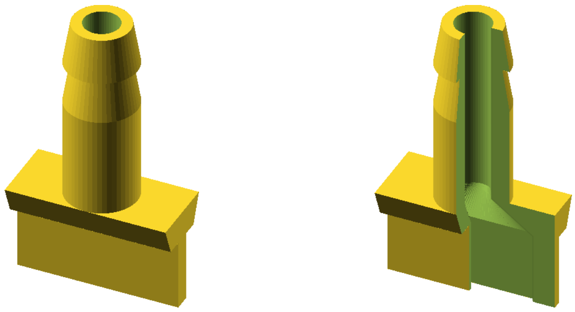

(a) Outside **(b)** Cutaway view

Figure 5.5: 3D rendering of the monolithic gas inlet design.

we opted to have this design 3D printed. We were the first at our department to use this new technology, so to get an idea of the possibilities of the different materials available, we ordered a few samples in laser sintered plastic and UV cured resin at two companies: Sculpteo[4] and Shapeways[5]. Due to the very thin wall in the initial design, Sculpteo would only print in laser sintered plastic, while Shapeways would only print in the UV cured resin. After receiving the prints and removing the remaining material from the cavity, we found that while the UV cured resin is superior in terms of detail, the laser sintered plastic was stronger. Due to the fine detail of the spacer, the resin print walls easily cracked and were bent. The thin walls in sintered plastic were more resilient, but lacked the necessary level of detail.

Taking the shortcomings of the first design into account, we decided to design a second gas inlet, shown in Figure 5.6. To circumvent the thin walls, we opted for a gas port of the full gap width, i.e. 1.2 mm, while providing sufficient surface for adhesion to the glass further away from the port. This is to prevent glue from flowing into the port when the inlet is glued to the glass, which might obstruct gas flow once dried. The additional surface is mainly provided by the large wall, visible at the bottom in Figure 5.6d. The first glass sheet can then be inserted between this wall and the two smaller spacers also visible in Figure 5.6d. Figure 5.6a and Figure 5.6b show the tapering applied to these protrusions, which ensures that the glass will be self centering when it is glued in.

The second glass sheet does not have to be slid in, but can be put in from the top. This provides the possibility of glueing all the spacers to one sheet of glass first, and then only put the second sheet in when the glue has dried and everything is fixed in place. A small groove is also provided for the second glass sheet. The sheet itself will be glued on top of the two spacer, so to ensure gas tightness some glue can be applied in the groove after the sheet has been put in place, again to prevent glue from flowing into the gas port.

The gas tube fitting can be glued into the provided opening, just like with the CMS gaps. We chose for a two-part design since this saves some material for the 3D printing, and thus reduces the cost of the inlet adapters. The hole for the fitting is 0.2 mm wider than the fitting itself, to allow some space for the glue. The fitting is not glued in using two-component glue, but the much faster curing cyanoacrylate. To ensure enough room is available for the gas tube, which will run along the edge of the gap, 2.5 mm of space was provided between the edge of the glass sheet and the tube fitting. It is best to only glue the tube fitting in *after* the gap has been sealed and finished with silicone. This reduces the risk of it breaking and eases the application of the silicone next to the inlet adapter.

The final design of the gas inlet adapter allows two adapters to be placed on opposite corners of the gaps. Both gaps are to be constructed in an identical way, such that when both cathode plates are facing each other, no part of the inlet adapters is in between the gaps, and the gas tube fittings are directed towards each other. This allows for an easy connection of the output of the first gap, to the input of the second gap on one side of the chamber (see also section 5.2.5).

5.2.2 Gas flow

The positioning of gas inlet and outlet on opposite corners of the gap was assumed to force the gas flow diagonally across the gap, which would ensure efficient distribution of fresh gas in the active central

[4] Sculpteo, 89 rue Gouverneur Eboué, 92130 Issy-les-Moulineau, France (`http://www.sculpteo.com`)
[5] Shapeways NL, Hastelweg 222, 5652 CL Eindhoven, The Netherlands (`http://www.shapeways.com`)

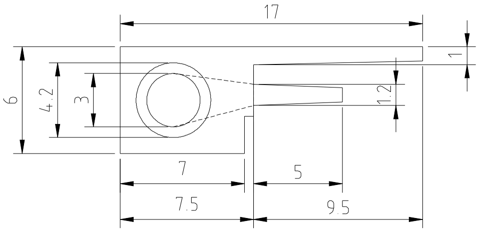

(a) XY projection

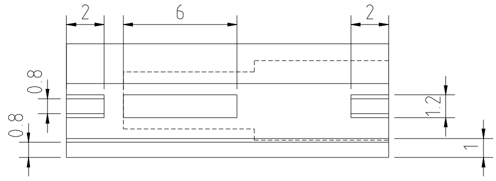

(b) YZ projection

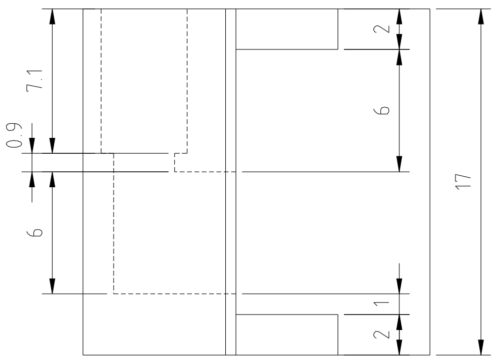

(c) XZ projection

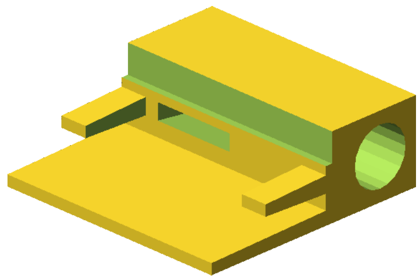

(d) 3D rendering

Figure 5.6: Projections of the gas inlet adapter. Dashed lines indicate boundaries of hollow inside. Dimensions are in mm.

region of the gap. Prior to construction of the gaps, no simulations were performed however to confirm this view.

Using on the time needed to flush a gap layer used in the CMS RE/4/3 chambers, one may calculate the number of gap volumes n_V that is put through the gap before it is considered ready for testing or operation. This can be done using equation (5.1), where V is the internal gap volume, and f the gas flow that is fed into the gas. With $f_{\mathrm{CMS}} = 5\,\mathrm{l\,h^{-1}}$ and $t_{\mathrm{CMS}} = 24\,\mathrm{h}$, one finds that the equivalent flushing time for our gaps is 3 h, employing a flow of $1\,\mathrm{l\,h^{-1}}$. Note that this is equivalent to an n_V of nearly 30. Despite this large value, we found that after 3 h, the dark current drawn by the gap was still larger than expected at low high voltage values ($< 6\,\mathrm{kV}$). This was likely due to premature breakdown of the gas mixture inside the gap, due to remaining air.

$$n_V = \frac{f}{V} \times t \tag{5.1}$$

First of all, equation (5.1) does not take the tubing into account that connects the gap to the gas system, which amounts to a volume V_0 of ca. ($6\,\mathrm{m} \times 12.6\,\mathrm{ml\,m^{-1}}$), only counting the tubing *to* the gap. If the input from the gas system has been open to air, the gaps thus need to be flushed for at least $\frac{V_0}{f}$ to flush the air from the tubing. However, even at a flow rate of $1\,\mathrm{l\,h^{-1}}$, this only amounts to an additional flushing time of less than 5 min.

Secondly, a simulation has been performed of the in-gap gas flow, to test the assumption of diagonal flow. The simulation was performed using Gerris[6], and consisted of an approximate two dimensional representation of a `GHENT-GRPC-01` gap with gas inlet and outlet at opposite corners. To simplify the geometrical description, some small details such as short pieces of strip spacers, and the ball spacers, were left out. The flow in the plane of the gap is expected to be laminar, which should allow a reduction to a 2D simulation to be made. As is common in simulations, the employed units are relative to the configuration. The velocity of the gas v is normalised to the velocity of the inflowing gas ϕ, given by

[6]Gerris allows solving of two or three dimensional fluid dynamics problems. It employs an adaptive spatial and temporal grid, to automatically resolve detailed features of the flow, or coarsen the simulation whenever possible to reduce computational cost. A full description of the software is given by Popinet [50].

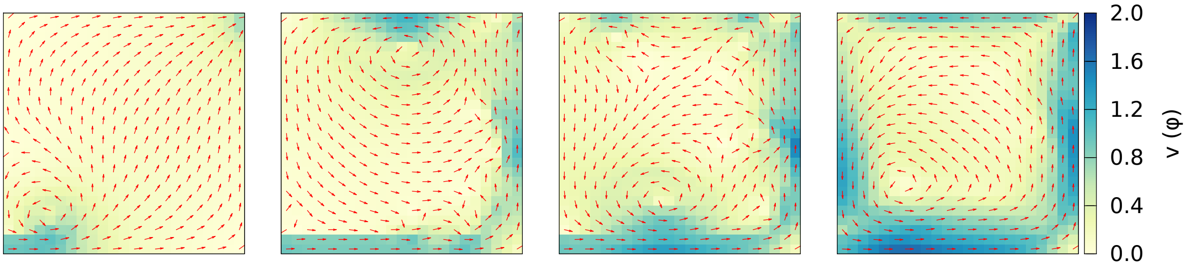

(a) T = 0.09τ (b) T = 0.52τ (c) T = 0.87τ (d) T = 3.48τ

Figure 5.7: In-gap gas flow simulation of the `GHENT-GRPC-01` gaps. Units are normalised to the gap volume and velocity of the inflowing gas. Arrows indicate the flow direction of the gas, while the gas velocity is colour mapped using the scale on the right. The inlet is positioned in the bottom left corner, the outlet in the top right corner.

equation (5.2a), where A is the cross section of the inlet opening. Time is normalised to the time τ it takes to insert one gap volume of gas.

$$\phi = fA^{-1} \tag{5.2a}$$

$$\tau = Vf^{-1} \tag{5.2b}$$

Results of the simulation are shown in Figure 5.7. The initial gas flow in Figure 5.7a can be seen to remain close to the sides, resulting in a single convection cell inside the gap, visible in Figure 5.7d. Refreshing of the gas in the active central part of the detector, is thus mainly diffusive. If air is still present inside the gap, then the difference in density of the employed gas mixture (4.2 g/l) and air (1.2 g/l) will also induce some mixing, although this depends on the orientation of the gap.

One possible solution to improve the gas flow inside the gap, is to provide a ‘distribution channel’, as is done by e.g. Bedjidian et al. [13]. The single gas input of the gap is then first fed into a channel, from where the gas can be distributed more uniformly through multiple holes along the edge of the active volume.

5.2.3 High voltage connection

The resistive coating of the prototype has already been discussed extensively in section 3.5. After assembling the gap, the high voltage connection to the electrodes still has to be provided. This is done by glueing a strip of copper foil to the edge of the coating, preferably centred on one of the read-out strips to prevent charge spreading. This was done with conductive two-component glue [37]. The read-out strips should be positioned as close to the anode as possible, so we will use negative high voltage and keep the anode grounded. This minimises the voltage difference between the anode and the adjacent read-out strips, thus minimising the risk of possibly harmful sparks. The copper patch for the anode, shown in Figure 5.8b, is folded just over the edge of the gap. The ground wire itself is then soldered onto the copper along the edge of the gap. Additional thickness is less of a problem for the cathode, so here the wire is just soldered to the copper on top of the gap, which is still visible underneath the yellow electrical tape in Figure 5.8a. The tape provides extra fixation of the wires strips, while ensuring insulation of the two contacts.

Properties of the high voltage and ground wiring are listed in Table 5.3. The two wires are assembled into a Jupiter connector, pictured in Figure 5.8c, once again for compatibility with the existing setup. The cabling is furthermore protected with a double layered braided sleeve. The inside sleeve is metallic and shields the power supply from external noise, while the plastic outside sleeve provides electrical insulation.

5.2.4 Signal read-out

Much like the CMS RPCs we will employ a double gap structure with read-out strips inbetween the gaps. Not being tied to geometrical constraints like the CMS strip patterns described in section 2.4.1 however,

(a) HV wire **(b)** Ground wire **(c)** Jupiter connector

Figure 5.8: High voltage connection of the gaps. The HV wire (a) is placed on top of the gap, while the ground wire (b) is placed on the edge of the gap. The wires are soldered to a piece of copper foil that is glued to the resistive coating, and fixed in place using electrical tape (yellow). Both wires go to the high voltage connector (c) through a sleeve (grey) that is fixed with thermal shrink (black).

Table 5.3: Properties of the wiring used for construction of the gRPC prototype.

Wire	Voltage rating	Insulator	Farnell article number
HV	15 kV DC	Silicone	18 43 258
GND	300 V AC	Silicone	14 65 869

we went for the easy option of carefully applying pieces of copper tape to a Mylar sheet. With a tape width of 25 mm and a strip spacing of 2 mm, resulting in a strip pitch of 27 mm, we applied 10 read-out strips. Using a Mylar foil of the same width as the glass, i.e. 30 cm, this leaves an empty edge of 16 mm on both sides, a distance that was also maintained at the end of the strips, as can be seen in Figure 5.9a. Since the coating is applied 25 mm from the edges, this leaves 9 mm of dead strip space on all sides.

The copper strips are isolated from the gap electrodes by a sheet of Mylar on both sides. The top foil is just the size of the gaps, while the bottom foil is 31 cm long, so that the wires to connect the strips with the read-out electronics, are not between the gaps. In this way, both gaps can be placed as close as possible to the strips, which should minimize the cluster size. In Figure 5.9b and Figure 5.10 one can see that these coaxial read-out wires are soldered to the strips and the copper shielding foil. The shielding is used to reduce the amount of external noise picked up by the strips by almost completely wrapping the gaps.

The read-out wires lead to an adapter board, indicated in Figure 5.10, that can be connected to a CMS FEB. This board contains the old electronics discussed in section 4.1. We did not yet employ the new read-out electronics, as we did not have sufficient electronics for 10 channels, thus requiring the use of CMS electronics in any case.

(a) Strip pattern **(b)** Read-out wires

Figure 5.9: Pictures of the strip pattern and wires to connect the strips to the read-out electronics. Also visible are (a) the yellow electrical tape attaching a second Mylar sheet cover for electrical insulation, and (b) the copper shielding foil.

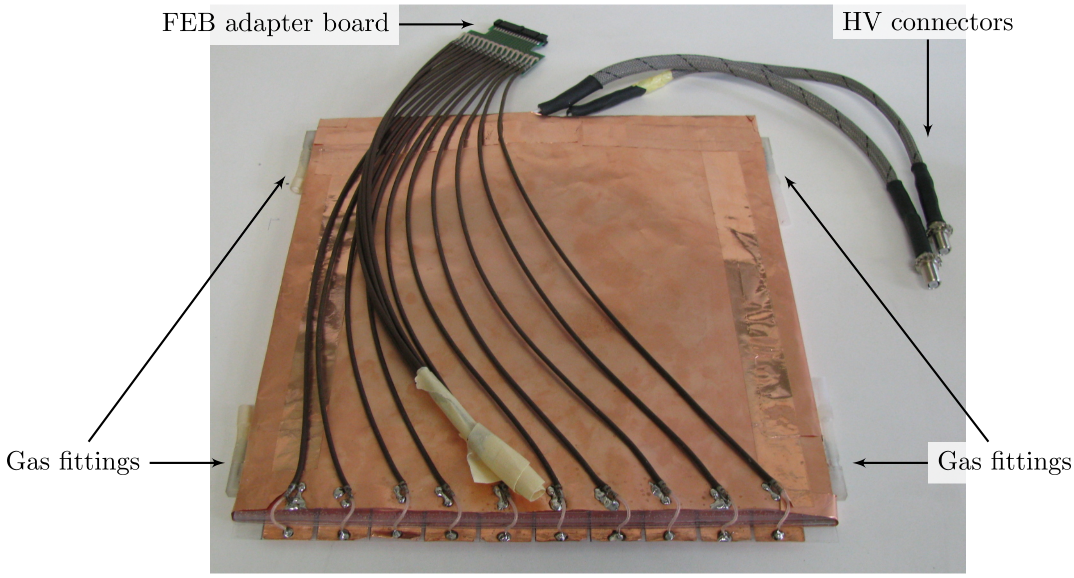

Figure 5.10: Shielded double gap structure. Several connections have been annotated. Also visible are the ends of the strips, sticking out from between the gaps, as well as six unused read-out wires taped together.

5.2.5 Double gap casing

Based on the RE/4/3 chambers, an enclose for our prototype gap was designed by A. Fagot. Unlike the CMS chambers, we will not use honeycomb panels[7] for the large sheets, but plain aluminium as it is more easily available. The circumference of the casing consists of aluminium bars, to which the top and bottom plate are screwed. Inside the casing, the gap is secured by several L-pieces, screwed to the bottom plate.

At one side, a gas tube will connect the outlet of the first gap to the inlet of the second gap, while at the opposing side, tubes connected to the other inlet and outlet will be directed outward through the top plate. Together with the two high voltage connectors, the gas input and output pipes will be placed on a small patch panel on the top of the case.

The aluminium sheets will be milled to accommodate for the outside walls of the gas inlet adapters and the high voltage connection on the anode plates, wherever this is necessary. In this way, the glass plates will receive maximum support of the case, while pressure is evenly divided across the surface of the gap. This also ensures that the gaps will be pressed firmly against the central strips, to improve read-out.

As of 15 June, 2013, the construction casing is not yet completed, so the double gap structure has not been installed yet.

5.3 Prototype characterisation

We designed the gRPC prototype for maximum compatibility with existing CMS RPC testing infrastructure in Ghent. In this way, we could easily perform tests on the gas tightness [58] and on the high voltage performance [30] of our gaps. After ensuring proper operation, the gaps can be assembled into a complete chamber, to determine the detection efficiency of our prototype, again using only the setup available for testing of the RE/4/3 chambers.

5.3.1 Gas tightness

A first preliminary leak test was performed after completely assembling the first gap, but before the silicone was applied. An overpressure of 5 mbar disappeared in a matter of seconds, which we were able

[7]Honeycomb panels consist of an aluminium honeycomb pattern, filled with foam. It is closed of by bars at its edges, and laminated with thin plates on the top and bottom sides. Due to its structure and composition, it provides sufficient rigidity to the chambers, while maintaining a low density, thus reducing the amount 'dead material' in the detector.

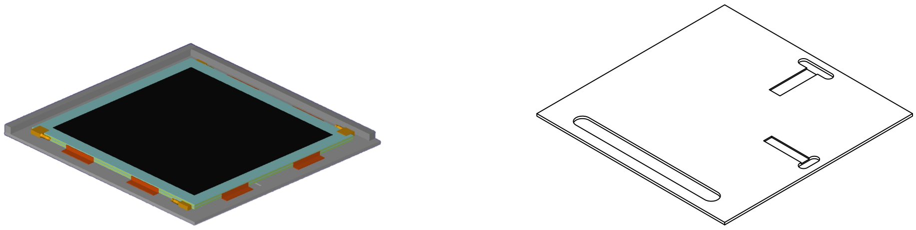

(a) Opened up **(b)** Top cover

Figure 5.11: Drawings of the case design for the small gRPC prototype. An opened up rendering of the case (a) shows the inside parts. Shown are the coated gaps (blue/black), gas inlets (orange), L-bars (brown), and the outside aluminium casing (grey). The top cover of the case (b) has holes for the gas (bottom right), high voltage (top), and strip read-out (left). By A. Fagot.

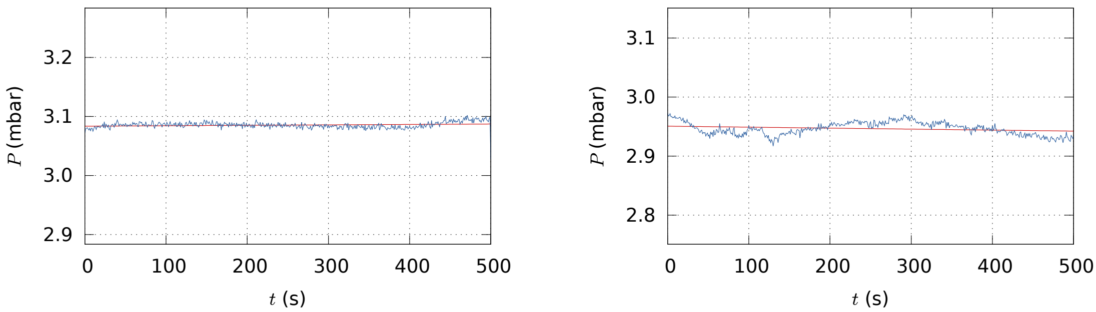

(a) `GHENT-GRPC-01-001` **(b)** `GHENT-GRPC-01-002`

Figure 5.12: Leak test of the prototype gaps. The measured pressure is shown in blue, the red line indicates the linear leak rate fit.

to fix by applying the silicone.

The full leak test procedure is based on the one used for the RE/4/3 gaps. First of all, one has to ensure that the gap has the same temperature as the surrounding environment, so one should not move it from another room to the test setup, just before doing the leak tests. Once it's temperature is stable, the overpressure inside the gap can be increased to 3 mbar. One then waits 600 s for the pressure to stabilize. Finally, the pressure is monitored during an additional 500 s, which provides the data used for the calculation of the leak rate L.

The results for both prototype gaps are shown in Figure 5.12. Assuming a linear decay of the overpressure, L_i is derived from a fit to the data. Equation (5.3a) gives the fitted leak rate of the first gap (Figure 5.12a) and can be seen to be negative, i.e. the pressure increases over time. This was most likely due to heating up of the gap during the leak test, but nevertheless it shows that the gap is gas tight at 3 mbar. For the second gap (Figure 5.12b), we ensured that the gap was at the same temperature as its surroundings, i.e. that the pressure did not increase over time. The leak rate for the second gap is given by equation (5.3b).

$$L_1 = (-0.44 \pm 0.09)\,\mu\text{bar/min} \tag{5.3a}$$
$$L_2 = (1.0 \pm 0.2)\,\mu\text{bar/min} \tag{5.3b}$$

During assembly of the second gap, one of the metal bars used to apply pressure tipped over. This caused one of the glass sheet corners to shatter, with one of the cracks running across the edge of the gas volume, although the strip spacer did hold all the pieces together. A thin layer of silicone was applied on top of the cracks, and the gap was otherwise assembled as described above. The leak test shows that the cracked glass sheet has little or no influence on the gas tightness, and the gap has not shown to perform less than the other gap.

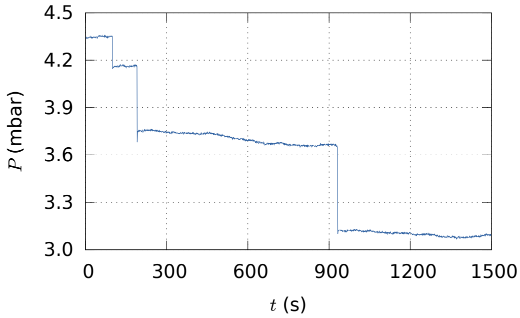

Figure 5.13: Leak test of `GHENT-GRPC-01-002` at 5 mbar showing popping spacers as sudden drops in pressure.

The leak tests for the RE/4/3 gaps are performed at 5 mbar and 20 mbar overpressure. However, these gaps employ disc-shaped spacers so the glue connection is stronger. With our ball spacers there was only a very small surface glued to the spacers, causing the spacers to 'pop' if too large an overpressure is applied to the gaps. Attempting to perform a leak test at 5 mbar has caused at least some of the spacers to pop. Figure 5.13 shows the popping in the second gap as sudden drops in pressure, while the pressure is otherwise stable.

5.3.2 Dark currents

The current a gap draws when it is powered, but not exposed to radiation, is called the dark current. This current is the combination of amplified ionisation of the gas, e.g. due to cosmic rays, and electrons emitted from the cathode, as well as leak currents due to a finite conductance of the gap elements separating the two resistive plates. This current should preferably be low, such that the power requirement and heat production of the RPC remains acceptable. A fully equipped RPC system at CMS would have a surface area of $3416\,\mathrm{m}^2$ [54]. At an operational power consumption of $3\,\mathrm{W/m}^2$, this would mean the RPCs alone would already require 10 kW. Note that this is only the power required to run the detector, a sufficient cooling system has to be present too, to keep the temperature within acceptable limits.

The results of the dark current test for the two prototype gaps, over a voltage range of 1 kV to 8 kV, are shown in Figure 5.14. For this test we used the CMS gas mixture described in section 2.4, with a relative humidity of 20 % to 40 %. The active surface of these prototype gaps is only $(25 \times 25)\,\mathrm{cm}^2$, which is small compared to the CMS gaps, hence the lower resolution for the current per surface area (see Figure 4.8). After the new voltage is set, the current is monitored during 15 min to allow the gap to charge, and the current to settle down to its steady-state value. The measured current is the mean value over these 15 min.

Up to ca. 7 kV, the measurements agree reasonably well with the dark current drawn by the RE/2/2 gaps used in the electronics tests. Starting from 7 kV, the currents can be seen to sharply increase. Being linear, this rise could be ohmic conduction due to breakdown of the gas. Equation (5.4) can be fit to each of the curves in Figure 5.14 for $V > 7.6\,\mathrm{kV}$, where g is still the gap width.

$$I(V) = \frac{(V - gE_c)}{R} \tag{5.4}$$

Equation (5.4) has been fitted to the two curves in Figure 5.14, for $HV_{\mathit{eff}} \geq 7.6\,\mathrm{kV}$, after subtracting the initial exponential rise. The weighted averages of the fitted parameters are given by equation (5.5a) and equation (5.5b), for the critical field strength E_c and resistance after breakdown R respectively. Indeed, comparing the critical field to the value of $5.3\,\mathrm{kV\,mm^{-1}}$ for the main component of the used mixture (R134a), given by McAllister [45], shows that the rise in conductance is likely due to gas breakdown, which is delayed by the presence of iC_4H_{10} and SF_6.

$$E_c = (6.26 \pm 0.03)\,\mathrm{kV\,mm^{-1}} \tag{5.5a}$$
$$R = (2.75 \pm 0.07)\,\mathrm{G\Omega} \tag{5.5b}$$

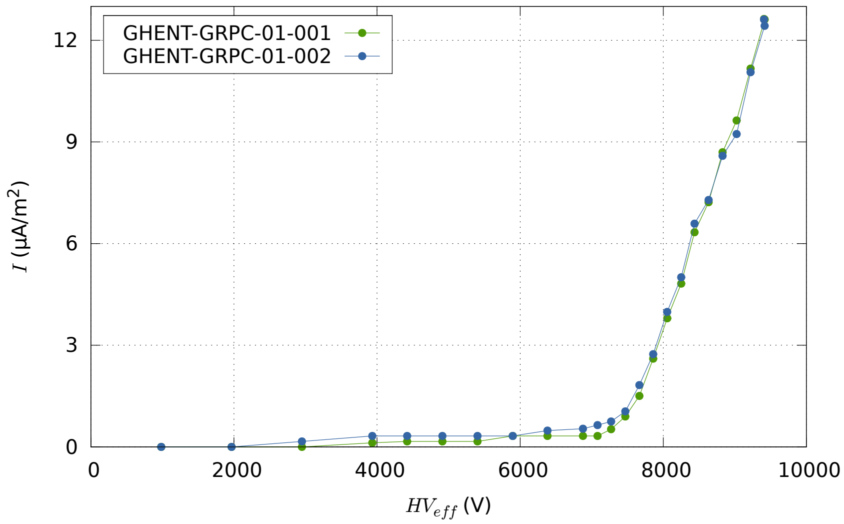

Figure 5.14: Dark current test of the prototype gaps.

5.3.3 Detection efficiency

After completing the tests on the individual gaps, we proceeded by joining the two gaps with the intermediate strip layer, and shielding them. The supplies for the full casing had not been delivered yet, so the first double gap tests had to be performed with only the copper shielding. The (partially) assembled prototype, as shown in Figure 5.10, was then placed in the cosmic stand to perform a high voltage scan of the detection efficiency. The cosmic stand consist of two layers of independent scintillator strips[8] for triggering, one 130 cm above the other. RPC chambers can be placed between these trigger layers, in one of the five stations. Alternatively, one can place a RPC in the topmost and bottommost station, which can then serve as a more efficient trigger. This is indeed done with the RE/4/3 chambers, where two units are then used as a trigger, and up to three other units are under test. This also allows for more precise tracking of cosmic rays, and an efficiency determination per segment, or even per strip. For our tests, we did not use a RPC trigger, but restricted the scintillator trigger to the four centremost strips.

A basic Monte Carlo simulation was performed to determine the geometric acceptance α_g of the gRPC in the cosmic stand, i.e. the fraction of cosmic rays (that generate a trigger) that pass through the active volume of our prototype. The actual detection efficiency ϵ can then be derived from the measured efficiency ϵ_m using equation (5.6). Generation of events uses an angular distribution of cosmic rays that is proportional to $\cos^2\theta$, where θ is the zenith angle [16].

$$\epsilon = \frac{\epsilon_m}{\alpha_g} \tag{5.6}$$

In the simulation the trigger layers and gRPC are assumed to have zero thickness. The prototype is 5 cm from the edge of the scintillators in the long direction, centred in the other direction, and is 80 cm below the top scintillator layer. An estimate was also made of the acceptance variation for small (< 5 cm) deviations of the assumed alignment. The results of the calculations are given by equation (5.7).

$$\alpha_g = 8.5\,\% \tag{5.7a}$$

$$\nabla\alpha_g = 0.23\,\%\,\mathrm{cm}^{-1} \tag{5.7b}$$

Data acquisition at the cosmic stand has been described extensively by Cornelis [30]. In short, coincidence of the top and bottom trigger provides a gate signal for the time-to-digital converter (TDC)

[8]The scintillators are 2 cm thick, and have a horizontal surface area of $(200 \times 10)\,\mathrm{cm}^2$. A characterisation of these strips was performed by Cornelis [30].

Table 5.4: Fitted parameter values for the GHENT-GRPC-01-C01 efficiency measurement.

ϵ_m^{max}	HV_{50} (V)	λ (V^{-1})	HV_{WP} (V)
0.164 ± 0.004	6018 ± 15	0.0078 ± 0.0006	6550 ± 30

module that determines the arrival time of all the signals from the individual scintillators and RPC read-out strips. These arrival times are then saved in a time window around the trigger, so also signals that arrive a certain amount of time before or after the trigger signal are recorded. In this way, the timing difference between the trigger signals and RPC signals does not need to be taken into account during data acquisition. It also allows for an estimate of the strip noise to be made, by counting the read-out signals that arrive (well) before the actual trigger signal. For example, in our measurements one of the strips was continuously generating signals. By discarding any signals from this strip in the analysis, a proper measurement could nevertheless be obtained. A possibly relevant detail is that the 'hot strip' covered both two of the ball spacers, as well as one of the high voltage connections. The other two strips that cover either of these features show no excessive noise however, so the noise is more likely caused by something else.

In the analysis of the data, a Gaussian distribution is the fit to the timing spectrum of the RPC read-out signals, which allows one to select only events with a 'good timing.' After testing different timing cuts around the peak value μ of the Gaussian, it was found that employing a window width of four times the standard deviation σ, i.e. $t \in [\mu - 2\sigma, \mu + 2\sigma]$, effectively selects the real signal. Subsequently, the RPC read-out signals with good timing are analysed for the following characteristics:

1. Hit multiplicity: total number of strips firing,
2. Cluster sizes: number of adjacent strips firing, and
3. Cluster count: number of clusters per event.

Clean signals are then defined for the scintillators and the read-out strips. A 'clean trigger' denotes that the hit multiplicity in both scintillator layers is one, while a 'clean detection' is a RPC signal with unit cluster count. The detection efficiency ϵ_m can then be calculated by dividing the total number of clean detections by the number of clean triggers. Besides the signal registration, the environmental parameters needed to calculate HV_{eff} were also automatically logged. The measurements were then reshaped into the format required by the software described in section 4.2.2, to fit the sigmoid curve. The fit parameter values are shown in Table 5.4, while the measurements and the fit of the efficiency curve itself are shown in Figure 5.15.

First of all, one may note that ϵ_m^{max} is larger than the simulated maximum α_g. In fact, $\epsilon_m(2\alpha_g)^{-1}$ gives $\epsilon = 0.96 \pm 0.01$. Given the presence of the maximum efficiency plateau, and the similarity of the chamber to the CMS chambers, one indeed expects the maximum efficiency to be close to one. Despite thorough checks of both the acceptance simulation and the data processing code, no reason for the presence of the extra factor 2 has been found. Note also that due to disabling one of the strips in the analysis, the actual active surface does not correspond any longer to the simulation, but is slightly smaller. However, due to a (varying) finite size of the signal footprint, the actual loss of active surface is not easily determined.

Having employed the same gas mixture as the CMS gaps, and the CMS electronics with a ZCD threshold value of 215 mV, allows for a more straightforward comparison between the two RPC types. The difference in HV_{WP} is (2980 ± 40) V, but the electrical field is actually higher than at the working point of the Bakelite RPCs, due to the reduced distance over which the avalanche can develop. To maintain the same signal strength, the effective Townsend coefficient η thus has to be higher. This does influence the shape of charge spectrum however, which is related to ηg, resulting in a different value for λ. The faster the spectrum of q_{ind} unfolds above the detection threshold, the larger λ will be, thus the faster the chamber will turn on for increasing high voltage. Due to the unknown value of ϵ, the absolute efficiencies of the two chamber types yet cannot be compared.

The power used by the RE/2/2 chamber in the electronics test in chapter 4 was 1.5 mW/m^2. Multiplying HV_{WP} for our double gap gRPC, with the measured dark currents from Figure 5.14, gives a value of ca. 2.5 mW/m^2. During the efficiency scan, the currents were of course also monitored, the results of which are shown in Figure 5.16. These currents can be seen to be substantially higher than the earlier dark current measurements, though both scans rely on the same cosmic rays to induce the current flowing through the gas. The resulting power usage is thus also higher, with a value of ca. 13 mW/m^2.

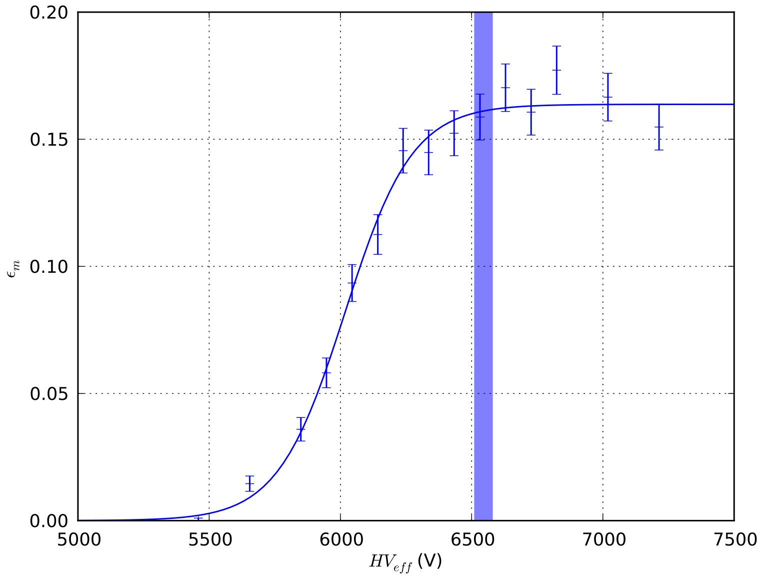

Figure 5.15: Measured detection efficiency scan for the `GHENT-GRPC-01-C01` chamber.

Most likely there are still some leakage currents across the surface and edges of the gap, e.g. via the unprotected parts of the conductive copper shielding.

5.4 Current state and future schedule

For the possible upgrade of the forward muon system in CMS, a short overview of the current state of the gRPC project in Ghent is presented in this section. We have designed a segmented gRPC as shown in Figure 5.1, to be constructed with the LRS glass developed at Tsinghua University. To tackle one problem at a time, the construction process has been divided into intermediate steps to allow the group here in Ghent to gain some experience with the construction of a gRPC.

As extensively discussed in section 5.2, a $(30 \times 30)\,\mathrm{cm}^2$ double gap gRPC has been constructed, using single sheets of float glass for the construction of the gaps. Using the testing equipment at the Ghent RPC-lab, the gaps were characterised and found to be performing well. Finally, an efficiency measurement was performed using the cosmic stand, which yielded a (relative) maximum efficiency of $(16.4 \pm 0.4)\,\%$. Due to a discrepancy with the Monte Carlo simulation of the geometrical acceptance, this measurement could not be normalised to an absolute detection efficiency, so further measurements are required to obtain this result.

The gaps are connected to the gas system using 3D printed, custom designed gas inlets. Due to an unexpected long flushing time of the gap, a basic simulation of the gas flow was performed, which showed the creation of a single convection cell, limiting the refresh rate of the gas located centrally in the RPC gaps. To circumvent this problem, a future gap design could include a distribution channel which feeds the gas into the main volume through several holes along on edge of the gap, creating a more uniform flow of gas inside the gap. Using the CMS gas mixture, breakdown occured at ca. 7.4 kV, which may or may not turn out to be a problem, depending on the required plateau width.

For a next iteration of the gRPC gaps, a segmented resistive plate will be tested. Using $(30 \times 30)\,\mathrm{cm}^2$ float glass sheets, which will be cut into four pieces and glued back together, the influence of the glue seams will be tested. Once this has been shown to work, it should be possible to proceed to the construction of a RE/4/1 gRPC using float glass. The final step will then be the construction of a full size detector using the LRS glass.

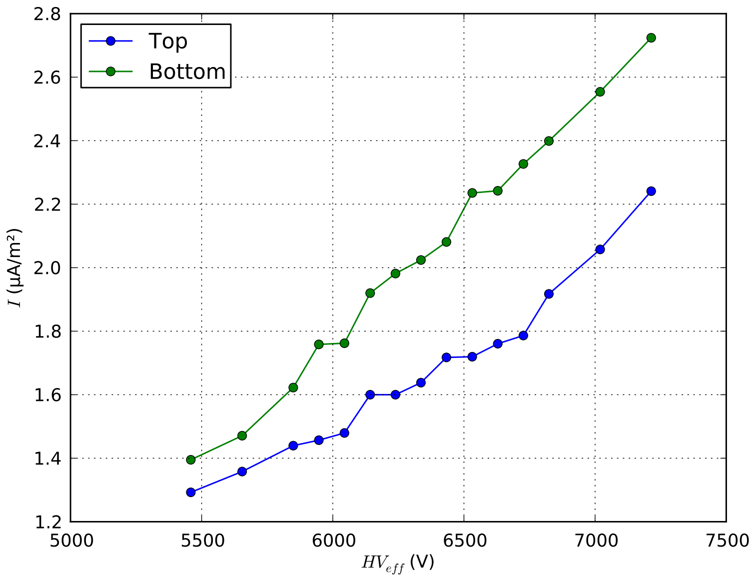

Figure 5.16: Monitored average gRPC gap currents during the efficiency scan.

Chapter 6

General conclusions

For the second upgrade of LHC, starting in 2018, an upgrade of the forward muon system of the CMS detector is being studied. For regions of high pseudorapidity, trigger detectors that can handle the high rates and integrated deposited charge are required. A glass resistive plate chamber constructed with semiconductive glass, developed at Tshinghua University, is one of the detector types under consideration. Ghent University therefore intends to construct a prototype detector of the RE/4/1 chamber geometry used by CMS, to study the feasibility of using a detector based on the semiconductive glass. In order to gain some experience on the construction of a resistive plate chamber, a small scale prototype employing normal float glass was constructed for this thesis.

For the resistive electrode coating, we strived to obtain sheet resistance of ca. $1\,\mathrm{M\Omega/\square}$. Making use of silk screen printing, a mixture of conductive and resistive paint was applied to the glass sheets and tested for uniformity. Using a conductive paint mass fraction of $16\,\%$, a mean sheet resistance of $0.7\,\mathrm{M\Omega/\square}$ was found, although the values showed a significant spread. This spread was found not to be Gaussian, suggesting that the current method of resistive coating application is insufficient and requires refinement. A coating procedure has been formulated, although it will likely have to be adjusted in the future, as the current infrastructure does not allow curing of surfaces of the dimensions required for the envisioned RE/4/1 prototype.

Besides operating a RPC in avalanche mode, and using semiconductive glass, another method of improving the rate capabilities is by employing a more sensitive preamplifier for the signals created by the detector. In this light, preliminary measurements were performed using a new sensitive preamplifier. Thanks to their design, these electronics can amplify fast, small signal without adding a significant amount of noise. As a result, the RPC can be operated at a lower high voltage, which leads to a reduced power consumption an extended lifetime. An reduction of $(460 \pm 30)\,\mathrm{V}$ of the working voltage was found for the existing CMS RPCs, with room for future improvements. Although more detailed measurements should still be performed, these preliminary measurements already showed very promising results.

Finally, a $(30 \times 30)\,\mathrm{cm}^2$ CMS-like double gap gRPC with a gap width of $1.2\,\mathrm{mm}$ was constructed. The prototype gaps employed the above described coating, but not yet the new preamplifiers. For maximum compatibility with the existing testing infrastructure for the CMS RE/4/3 gaps, custom gas inlets were designed, which were 3D printed in UV-cured acrylic plastic, thus avoiding the use of the more fragile capillary tubes commonly used for thin gaps such as ours. This allowed testing of the prototype gaps with a procedure similar to the one used for the RE/4/3 gaps. These characterisation tests showed that our gaps are gas tight, and show good dark current behaviour up to $7.4\,\mathrm{kV}$, at which point the gas inside the gaps starts to break down. Additionally, a basic simulation was performed of the gas flow inside the gap to determine the rate at which the gas in the active volume is refreshed. The simulation showed that a single convection cell is created inside the gap, such that the gas in the centre of the gap is nearly stationary. To ensure better refreshing of the gas, future gaps could employ a distribution channel. Finally, a detection efficiency measurement was performed, which showed that the constructed gRPC reaches a detection plateau at $(6.55 \pm 0.03)\,\mathrm{kV}$. An absolute efficiency could not yet be determined due to a discrepancy between the measurements and the Monte Carlo simulation of the geometric acceptance of the setup.

Having constructed the first functioning glass resistive plate chamber in Ghent, the first steps towards a RE/4/1 sized RPC employing semiconductive glass have been made. Combining this detector with a sensitive read-out should then allow a high rate detector to be constructed, suited for use in the forward detection regions of the CMS detector at a high luminosity LHC after 2018.

Hoofdstuk 7

Samenvatting

In 2018 zal de Large Hadron Collider (LHC) te CERN voor een tweede maal sluiten voor een opwaardering. Momenteel wordt de haalbaarheid van een verbetering en uitbreiding van het voorwaartse muonsysteem van de CMS detector bestudeerd. In de detectorregio's dichtbij de bundellijn zal de intensiteit van de straling namelijk nog hoger zijn dan voorheen, waardoor detectoren vereist zijn die geschikt zijn voor efficiënte detectie bij hoge deeltjestempo's en geaccumuleerde lading. Een van de opties die hiervoor momenteel bestudeerd worden, zijn *glass resisitive plate chambers* (gRPC's), gebouwd met halfgeleidend glas ontwikkeld aan de universiteit van Tsinghua (China). De universiteit van Gent beoogt daarom een prototype te bouwen, gebaseerd op de RE/4/1 RPC geometrie gebruikt door CMS, om de haalbaarheid van een RPC met halfgeleidend glas te bestuderen. Teneinde ervaring op te doen met de constructie van een gRPC, is voor deze thesis een kleiner prototype gebouwd, gebruik makende van gewoon vlakglas. Daar in Gent momenteel bijdraagt aan de assemblage RE/4/3 RPCs voor de uitbreiding van de CMS detector, kon deels gebruik gemaakt worden van de bestaande infrastructuur.

Een RPC bestaat uit twee vlakke platen, gemaakt van een slecht geleidend materiaal zoals bakeliet of glas, op een afstand van enkele millimeter van elkaar. Over deze korte afstand wordt vervolgens een hoogspanning aangelegd, resulterend in een elektrisch veld van ca. $5\,\mathrm{kV} \cdot \mathrm{mm}^{-1}$ in het geval van de CMS RPCs. Een resistieve laag — doch minder resistief dan het plaatmateriaal — wordt aan de buitenste zijden van beide platen aangebracht, zodat in het actieve volume een uniform elektrisch veld kan worden verkregen. Dit verzekert een constante werking van het apparaat over diens volledige oppervlak. Indien het gas in het interne volume van de detector nu geïoniseerd wordt door invallende straling, zorgt het aangelegde elektrisch veld ervoor dat de vrijgemaakte lading lawineversterking ondergaat. Deze lading kan vervolgens een signaal induceren op koperen stroken die tegen de anode van de RPC geplaatst zijn. Bemerk dat dit uitleessysteem verder volledig elektrisch gescheiden is van de RPC door middel van een isolerende kunststoffolie.

Het aanbrengen en karakteriseren van de resistieve coating was eerste aspect van de gRPC dat werd onderzocht. Er werd gepoogd een oppervlakteresistiviteit van $1\,\mathrm{M}\Omega/\square$ te behalen. Gebruik makende van een geleidende en resistieve verf werd een mengeling gemaakt, waarvan de geleidende verf een massapercentage had van 16 %. Via zeefdruk werd dan een resistieve laag aangebracht met een gemiddelde oppervlakteresistiviteit van $0{,}7\,\mathrm{M}\Omega/\square$, hoewel hierop veel spreiding zat. De waarden bleken echter niet Gaussisch verdeeld te zijn, wat de oorzaak van de spreiding naar alle waarschijnlijkheid bij de huidige aanbrengmethode plaats. Er werd een coatingprocedure geformuleerd, met aanbevelingen voor toekomstige verbetering. In ieder geval zal de procedure gewijzigd dienen te worden, daar de huidige infrastructuur niet toestaat (in een keer) een coating aan te brengen met de afmetingen van een RE/4/1-type RPC.

Naast het gebruik van halfgeleidend glas als constructiemateriaal, kan de maximale telcadans van een RPC verhoogd worden door gebruik te maken van elektronica die gevoeliger is voor kleine signalen. Enkele initiële metingen zijn daarom uitgevoerd met een nieuw type voorversterker. Dankzij haar ontwerp kan deze schakeling de snelle, kleine signalen van een RPC versterken, zonder een significante toename van de ruis. Bijgevolg is het mogelijk de detector te gebruiken bij met een lagere hoogspanning, zodat het verbruik en de veroudering verbeteren, terwijl de efficiëntie behouden blijft. De tests hebben aangetoond dat met de gebruikte opstelling een verlaging van $(460 \pm 30)\,\mathrm{V}$ mogelijk was. Hoewel meer uitgebreide metingen nog dienen te gebeuren, zijn deze resultaten alvast veelbelovend.

Uiteindelijk is dan een kleiner prototype gRPC van $(30 \times 30)\,\mathrm{cm}^2$ en een plaatafstand van 1,2 mm gebouwd. Hierbij is gebruik gemaakt van de hierboven beschreven coating, maar nog niet van de nieuwe voorversterker. Om compatibiliteit met de huidige testopstelling te verzekeren, zijn speciale inlaten ontworpen, die 3D geprint zijn in acryl dat uithardt bij blootstelling aan UV-licht. Zodoende kon het gebruik van de fragiele capillairen, die vaak gebruikt worden voor dit type van dunne RPC, vermeden worden en was aansluiting op het bestaande gassysteem eenvoudiger. Karakterisering van de prototypes is dan ook uitgevoerd met de bestaande opstelling in Gent, die gebruikt wordt voor de kwaliteitscontrole van de RE/4/3 RPCs. Deze tests hebben aangetoond dat de prototypes gasdicht zijn, en een goede donkerstroomkarakteristiek vertonen, waarbij vanaf 7,4 kV doorslag van het gebruikte gas werd waargenomen. Aanvullend is een simulatie uitgevoerd van de gasstroom binnenin de RPC. Hieruit is gebleken dat, door de plaatsing van de inlaten op overstaande hoeken van de detector, een convectiecel onstaat. Dit zorgt ervoor dat het gas dat zich centraal in de detector geen gedwongen verversing ondergaat, en de vermenging met nieuw gas hier dus vooral aangedreven wordt door diffusie. In het volledige RE/4/1 prototype zou dit verholpen kunnen worden door een distributiekanaal te voorzien binnenin de detector. Als laatste werd een efficiëntiemeting uitgevoerd, welke aangetoond heeft dat de gebouwde gRPC een plateau van maximale efficiëntie bereikt bij een hoogspanning van $(6{,}55 \pm 0{,}03)\,\mathrm{kV}$. Een absolute detectieefficiëntie kon nog niet bepaald worden doordat de Monte Carlo simulatie die de geometrische efficiëntie berekent niet overeen kwam met de meting.

Met de bouw van het een eerste werkend *glass resistive plate chamber* prototype hier in Gent, is een eerste stap gezet richting de bouw van een RPC met RE/4/1 afmetingen, gebruik makende van halfgeleidend glas. Het combineren van deze detector met gevoelige elektronica, zou dan een RPC moeten opleveren die geschikt is voor de voorwaartse detectieregio's van de CMS detector in aan toekomstige versie van de LHC versneller met hogere luminositeit na 2018.

Glossary

ASIC application-specific integrated circuit.

CERN Conseil Européen pour la Recherche Nucléaire.
CMS Compact Muon Solenoid.
CRP concentric ring probe.
CSC cathode strip chamber.
CSV comma separated values.

DT drift tube.

ECAL electromagnetic calorimeter.

FCA fast charge amplifier.
FEB front-end board.

gRPC glass resistive plate chamber.

HCAL hadronic calorimeter.

ILC International Linear Collider.

L1 First Level.
L2 Second Level.
LEP Large Electron–Positron Collider.
LHC Large Hadron Collider.
LRS low resistivity silicate.
LVDS low voltage differential signaling.

MB muon barrel.
ME muon end-cap.
mip minimum ionising particle.

PEEK Polyether ether ketone is a thermoplastic polymer, often used in high performance applications due to its mechanical strength.
PFA particle flow algorithm.
PMT photomultiplier tube.
pseudorapidity A coordinate used in detectors related to the angle with the beams.

RPC resistive plate chamber.

SLS soda-lime silicate.
SUSY supersymmetry.

TDC time-to-digital converter.

XML The 'Extensible Markup Language' allows data to be stored in a way that is readable for humans, and can also be easily processed by computer code.

ZCD zero-crossing discriminator.

Bibliography

[1] M. Abbrescia et al. „Cosmic ray tests of double-gap resistive plate chambers for the CMS experiment". In: *Nucl. Instrum. Meth. A* 550.1–2 (2005), pp. 116–126. DOI: 10.1016/j.nima.2005.06.074.

[2] M. Abbrescia et al. „Effect of the linseed oil surface treatment on the performance of resistive plate chambers". In: *Nucl. Instrum. Meth. A* 394.1–2 (1997), pp. 13–20. DOI: 10.1016/S0168-9002(97)00597-4.

[3] M. Abbrescia et al. „New developments on front-end electronics for the CMS Resistive Plate Chambers". In: *Nucl. Instrum. Meth. A* 456.1–2 (2000). Proceedings of the 5th Int. Workshop on Resistive Plate Chambers and Related Detectors, pp. 143–149. DOI: 10.1016/S0168-9002(00)00980-3.

[4] M. Abbrescia et al. „The simulation of resistive plate chambers in avalanche mode: charge spectra and efficiency". In: *Nucl. Instrum. Meth. A* 431.3 (1999), pp. 413–427. DOI: 10.1016/S0168-9002(99)00374-5.

[5] *Acheson Electrodag® 6017 SS.* Carbon-based polymer thick film ink. Nijverheidsstraat 7, B-2260 Westerloo, Belgium.

[6] *Acheson Electrodag® PM-404.* Resistive PTF ink; for resistive applications on polyester film. Nijverheidsstraat 7, B-2260 Westerloo, Belgium.

[7] C. Adloff. „CALICE Report to the DESY Physics Research Committee". In: *ArXiv e-prints* (2011). arXiv:1105.0511 [physics.ins-det].

[8] Z. Aftab et al. *Geometrical Layout and Mechanical details of CMS End Cap RPCs.* CMS Internal Note. Nov. 2002.

[9] M. Angelone et al. „Neutron Spectroscopy by Means of Artificial Diamond Detectors Using a Remote Read Out Scheme". In: *IEEE T. Nucl. Sci.* 57.6 (Dec. 2010), pp. 3655–3660. DOI: 10.1109/TNS.2010.2073484.

[10] *Araldite® 2011.* Klybeckstrasse 200, 4057 Basel, Switzerland, Apr. 2007.

[11] G. Battistoni et al. „Resistive cathode transparency". In: *Nucl. Instrum. Meth.* 202.3 (1982), pp. 459–464. DOI: 10.1016/0167-5087(82)90540-3.

[12] G. L. Bayatian et al. *CMS Physics: Technical Design Report Volume 1: Detector Performance and Software.* Technical Design Report CMS. Geneva: CERN, 2006.

[13] M. Bedjidian et al. „Glass resistive plate chambers for a semi-digital HCAL". In: *Nucl. Instrum. Meth. A* 623.1 (2010). 1st International Conference on Technology and Instrumentation in Particle Physics, pp. 120–122. DOI: 10.1016/j.nima.2010.02.168.

[14] M. Bedjidian et al. „Performance of Glass Resistive Plate Chambers for a high granularity semi-digital calorimeter". In: *J. Instrum.* 6 (2011), pp. –02001. DOI: 10.1088/1748-0221/6/02/P02001. arXiv:1011.5969 [physics.ins-det].

[15] L. Berger. „CRC Handbook of Chemistry and Physics". In: ed. by D. R. Lide. 85th ed. 2000 N. W. Corporate Blvd., Boca Raton (FL 33431), USA: CRC Press LLC, 2000. Chap. Dielectric strength of insulating materials, pp. 2451–2456.

[16] J. Beringer et al. „Review of Particle Physics". In: *Phys. Rev. D* 86.1 (July 2012), p. 010001. DOI: 10.1103/PhysRevD.86.010001.

[17] P. T. Boggs et al. „Algorithm 676: ODRPACK: software for weighted orthogonal distance regression". In: *ACM T. Math. Software* 15.4 (Dec. 1989), pp. 348–364. DOI: 10.1145/76909.76913.

[18] M. Bogomilov et al. „The HARP RPC time-of-flight system". In: *Nucl. Instrum. Meth. A* 508.1–2 (2003). Proceedings of the Sixth International Workshop on Resistive Plate Chambers and Related Detectors, pp. 152–158. DOI: 10.1016/S0168-9002(03)01342-1.

[19] Bohle. *Glass Processing.* Nieuweweg Noord 314 B-20, 3905 LX Veenendaal, The Netherlands, 2012.

[20] J. Brau et al. *International Linear Collider reference design report: ILC Global Design Effort and World Wide Study.* Geneva: CERN, 2007.

[21] *CAF® 4: Flexible adhesive for performance assembly.* Technical Data Sheet no. SIL 03 013 3. Feb. 2004.

[22] S. Callier et al. „HARDROC1, readout chip of the Digital HAdronic CALorimeter of ILC". In: *Nuclear Science Symposium Conference Record, 2007. NSS '07. IEEE.* Vol. 3. 2007, pp. 1851–1856. DOI: 10.1109/NSSMIC.2007.4436518.

[23] P. Camarri et al. „Streamer suppression with SF_6 in RPCs operated in avalanche mode". In: *Nucl. Instrum. Meth. A* 414.2–3 (1998), pp. 317–324. DOI: 10.1016/S0168-9002(98)00576-2.

[24] R. Cardarelli et al. „Avalanche and streamer mode operation of resistive plate chambers". In: *Nucl. Instrum. Meth. A* 382.3 (1996), pp. 470–474. DOI: 10.1016/S0168-9002(96)00811-X.

[25] R. Cardarelli et al. „Performance of RPCs and diamond detectors using a new very fast low noise preamplifier". In: *J. Instrum.* 8.01 (2013), pp. –01003.

[26] R. Cardarelli et al. „High rate fast precision tracking trigger with RPCs". In: *Proc. Sci.* RPC2012 (2012), p. 069.

[27] S. Chatrchyan et al. „Observation of a new boson at a mass of 125 GeV with the CMS experiment at the LHC". In: *Phys. Lett. B* 716.1 (2012), pp. 30–61. DOI: 10.1016/j.physletb.2012.08.021.

[28] A. Collaboration et al. „Electroweak Measurements in Electron-Positron Collisions at W-Boson-Pair Energies at LEP". In: *ArXiv e-prints* (2013). arXiv:1302.3415 [hep-ex].

[29] A. Collaboration et al. „Precision electroweak measurements on the Z resonance". In: *Phys. Rep.* 427.5–6 (2006), pp. 257–454. DOI: 10.1016/j.physrep.2005.12.006.

[30] T. Cornelis. „Design of a cosmic test bench for the quality control of Resistive Plate Chamber detectors for the CMS experiment". MA thesis. Universiteit Gent, Faculteit Wetenschappen, 2011.

[31] S. Costantini. *Calibration of the RPC working voltage in the CMS experiment.* Tech. rep. CMS-CR-2012-055. CERN-CMS-CR-2012-055. Geneva, Apr. 2012.

[32] L. Costrell et al., eds. *Standard NIM Instrumentation System.* DOE/ER-0457T. Washington, D.C. 20545: U.S. Department of Energy, May 1990. Chap. 5.9.3, p. 8.

[33] T. J. Coutts. „Percolation conduction in mixed insulator-conductor systems". In: *Thin Solid Films* 38.3 (1976), pp. 313–321. DOI: 10.1016/0040-6090(76)90009-2.

[34] I. Crotty et al. „Further studies of avalanche mode operation of resistive parallel plate chambers". In: *Nucl. Instrum. Meth. A* 346.1–2 (1994), pp. 107–113. DOI: 10.1016/0168-9002(94)90693-9.

[35] H. Czyrkowski et al. „New developments on resistive plate chambers for high rate operation". In: *Nucl. Instrum. Meth. A* 419.2–3 (1998), pp. 490–496. DOI: 10.1016/S0168-9002(98)00826-2.

[36] *Dow Corning® 3140 RTV COATING.* Rue Jules Bordet, 7180 Seneffe, Belgium, Feb. 2013.

[37] *EPO-TEK® EE129-4.* 7th ed. 14 Fortune Drive, Billerica (MA), USA, Dec. 2012.

[38] L. Evans and P. Bryant. „LHC Machine". In: *J. Instrum.* 3.08 (2008), pp. –08001. DOI: 10.1088/1748-0221/3/08/S08001.

[39] Y. Haddad et al. „High Rate Resistive Plate Chamber for LHC detector upgrades". In: *ArXiv e-prints* (2012). arXiv:1211.5698 [physics.ins-det].

[40] J. D. Hunter. „Matplotlib: A 2D graphics environment". In: *Comput. Sci. Eng.* 9.3 (2007), pp. 90–95.

[41] E. Jones et al. *SciPy: Open source scientific tools for Python.* 2001–.

[42] S. Kirkpatrick. „Percolation and Conduction". In: *Rev. Mod. Phys.* 45.4 (Oct. 1973), pp. 574–588. DOI: 10.1103/RevModPhys.45.574.

[43] G. F. Knoll. *Radiation Detection and Measurement.* 3rd ed. Wiley, 2000.

[44] *LEP design report Vol. II: The LEP main ring.* Copies shelved as reports in LEP, PS and SPS libraries. Geneva: CERN, 1984.

[45] I. W. McAllister. „The dielectric strength of 1,1,1,2-$C_2H_2F_4$ (Arcton 134a)". In: *J. Phys. D. Appl. Phys.* 22.11 (1989), p. 1783. DOI: 10.1088/0022-3727/22/11/035.

[46] M. Morales et al. „Conductivity and charge depletion aging of resistive electrodes for high rate RPCs". In: *J. Instrum.* 8.01 (2013), pp. –01022. DOI: 10.1088/1748-0221/8/01/P01022.

[47] F. V. Natrup et al. „Cation diffusion and ionic conductivity in soda-lime silicate glasses". In: *Phys. Chem. Chem. Phys.* 7.11 (2005), pp. 2279–2286. DOI: 10.1039/B502501J.

[48] P. Paolucci. „Test of different gas mixtures for RPC detectors." In: (1997).

[49] Y. N. Pestov et al. „Spark Counter With A Localized Discharge". In: (1978).

[50] S. Popinet. „Gerris: a tree-based adaptive solver for the incompressible Euler equations in complex geometries". In: *J. Comput. Phys.* 190.2 (2003), pp. 572–600. DOI: 10.1016/S0021-9991(03)00298-5.

[51] A. Ranieri. *A New Front-End Board for RPC Detector of CMS.* Tech. rep. CMS-NOTE-1999-047. Geneva, Aug. 1999.

[52] R. Santonico and R. Cardarelli. „Development of resistive plate counters". In: *Nucl. Instrum. Meth.* 187.2–3 (1981), pp. 377–380. DOI: 10.1016/0029-554X(81)90363-3.

[53] C. J. Schmidt and H. Risch. „Surface electrical conductivity of cured Araldite 2011 Epoxy System, a study initiated during Alice TRD production". In: *GSI Scientific report 2005.* Ed. by K. Große. Planckstr. 1, 64291 Darmstadt, Germany, 2006, p. 285.

[54] *The CMS muon project: Technical Design Report.* Technical Design Report CMS. Geneva: CERN, 1997.

[55] M. A. Thomson. „Particle flow calorimetry and the PandoraPFA algorithm". In: *Nucl. Instrum. Meth. A* 611.1 (2009), pp. 25–40. DOI: 10.1016/j.nima.2009.09.009.

[56] F. Thyssen. „Performance of the resistive plate chambers in the CMS experiment". In: *J. Instrum.* 7 (2012), p. C01104. DOI: 10.1088/1748-0221/7/01/C01104.

[57] M. Tytgat et al. „The Upgrade of the CMS RPC System during the First LHC Long Shutdown". In: *J. Instrum.* 8.02 (2013), T02002. DOI: 10.1088/1748-0221/8/02/T02002.

[58] M. Van Ginderachter. „Implementatie van een gassysteem voor de kwaliteitscontrole van Resistive Plate Chamber detectoren". MA thesis. Universiteit Gent, Faculteit Wetenschappen, 2011.

[59] J. Va'Vra. „Attempt to correlate the ionic model with observations in BaBar RPC chambers and R&D tests". In: *IEEE T. Nucl. Sci.* 51.5 (2004), pp. 2145–2150. DOI: 10.1109/TNS.2004.836063.

[60] J. Wang et al. „Development of multi-gap resistive plate chambers with low-resistive silicate glass electrodes for operation at high particle fluxes and large transported charges". In: *Nucl. Instrum. Meth. A* 621.1–3 (2010), pp. 151–156. DOI: 10.1016/j.nima.2010.04.056.

[61] Y. Wang et al. „Study on the performance of high rating MRPC". In: *Nuclear Science Symposium Conference Record, 2008. NSS '08. IEEE.* 2008, pp. 913–916. DOI: 10.1109/NSSMIC.2008.4774543.

[62] E. C. Zeballos et al. „Pure avalanche mode operation of a 2 mm gap resistive plate chamber". In: *Nucl. Instrum. Meth. A* 396.1–2 (1997), pp. 93–102. DOI: 10.1016/S0168-9002(97)00751-1.